Reprint from

Topics in Applied Physics

Volume 54: **Light Scattering in Solids IV**
Electronic Scattering, Spin Effects, SERS, and Morphic Effects
Editors: M. Cardona and G. Güntherodt

Springer-Verlag
Berlin Heidelberg New York Tokyo

8. Pressure-Raman Effects in Covalent and Molecular Solids

Bernard A. Weinstein and Richard Zallen

With 45 Figures

The advantages of pressure for studying solids have been recognized since the pioneering work of Bridgman. Hydrostatic pressure greater than a few kbar (1 kbar $= 10^9$ dyne/cm$^2 = 0.1$ Gigapascal) is a stronger and, in principle, a much cleaner perturbation than the more common thermodynamic variable temperature. For example, in Si a pressure of 100 kbar (easily attainable with modern techniques) produces a volume decrease of 5%, whereas the total temperature induced volume change in Si from 0 K to melting is only 1.8%. For the softer molecular solids this contrast is even greater. Furthermore, temperature is complicated by the parallel action of thermal expansion and phonon population effects, but hydrostatic pressure is manifest solely through volume change.

The main drawback of pressure studies is their experimental complexity. Expensive bulky apparatus are sometimes required, seals blow out, windows crack, and the sample size is necessarily small to achieve high pressure. Advances during the last decade, such as modern diamond anvil-type presses, have greatly reduced the mechanical problems. However sample size still remains small. Consequently, the importance of modern laser sources, which have catalyzed the general resurgence of Raman scattering, cannot be understated for pressure measurements. It is the marriage of modern laser-Raman and high-pressure techniques which has brought about the blossoming of pressure-Raman studies during the last decade. Though young, the marriage has been fruitful, and its future holds considerable promise.

The present review deals with two classes of solids, the tetrahedral semiconductors and the molecular insulators. Citations to work on other materials have been included in the references where appropriate. We begin by discussing the role of pressure in Raman processes and the Grüneisen parameter concept (Sect. 8.1). A brief account of experimental techniques follows (Sect. 8.2). Pressure-Raman studies of tetrahedral semiconductors (including materials from groups IV, III-V, II-VI, and I-VII) are then treated. This includes discussions of changes in phonon frequencies (Sect. 8.3), changes in phonon line shapes (Sect. 8.4), phase transitions (Sect. 8.5) and pressure-tuned resonant Raman scattering (Sect. 8.6). Our account of pressure-Raman effects in molecular solids (Sect. 8.7) is divided into five parts. These deal with overall rationale (Sect. 8.7.1), line shifts in simple organic and inorganic molecular solids (Sect. 8.7.2), vibrational scaling (Sect. 8.7.3), the connection between pressure and temperature effects (Sect. 8.7.4) and finally, molecular-to-non-

molecular transitions at high pressure (Sect. 8.7.5). Throughout we have limited the discussion to symmetry-conserving hydrostatic pressure investigations. Symmetry-breaking uniaxial stress studies are outside both the scope and space of this chapter. Nevertheless, for completeness some hydrostatic Grüneisen parameters deduced from uniaxial measurements have been included in Table 8.2 with appropriate citations, and a bibliography of recent uniaxial stress Raman work follows the numbered references.

8.1 The Raman Effect

Raman scattering is a powerful probe of solid-state excitations in the frequency range 3–3000 cm^{-1}. Pressure can cause large changes in the energies and interactions of these excitations within a given solid phase, and/or it can cause transitions to new phases having quite different excitation spectra. Let us examine formally how these changes manifest themselves in Raman scattering measurements.

8.1.1 How Pressure Enters

A typical experimental configuration is depicted schematically in Fig. 8.1. Here ω_l, ω_s, and ω_i are the angular frequencies of the incident laser photon, the scattered photon, and the elementary excitation under study, and $\boldsymbol{k}_l$, $\boldsymbol{k}_s$, and $\boldsymbol{q}_i$ are the corresponding wave vectors *within the scattering medium*. As usual, kinematics requires

$$\omega_l = \omega_s \pm \omega_i, \qquad \boldsymbol{k}_l = \boldsymbol{k}_s \pm \boldsymbol{q}_i. \tag{8.1}$$

In relating $\boldsymbol{k}_l$ and $\boldsymbol{k}_s$ to their counterparts *outside* the pressure vessel, one must properly account for the refractive indices of the optical windows and the pressure transmitting medium, which are, *of necessity*, part of the apparatus.

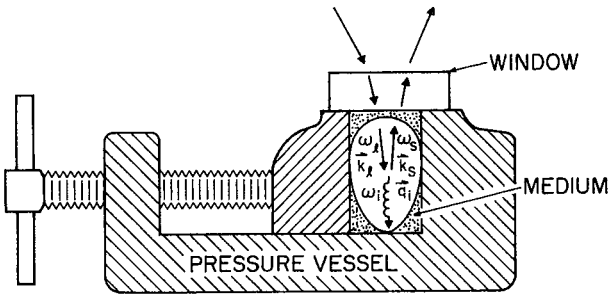

Fig. 8.1. Typical configuration for a hydrostatic pressure-Raman experiment in which a phonon ω_i, $\boldsymbol{q}_i$ is created (Stokes process). Of *necessity*, the window and medium are part of the sample chamber

Generally these indices will be pressure dependent and anisotropic so that the relationship will be nontrivial. In practice, this correction can often be neglected for Raman (but not Brillouin) studies because the dispersion relations $\omega_i(\boldsymbol{q}_i)$ are usually flat in the $\boldsymbol{q}_i \approx 0$ region of interest. However, if selection rules are to be tested closely, the correction should not be ignored. In that case the problem may still be circumvented for small energy excitations (typically valid to 1 % for $\omega_i \leq 200\ \mathrm{cm}^{-1}$) by arranging that the set of surfaces (window, medium, sample) traversed by the light are all parallel to the wave vector $\boldsymbol{q}_i$. It is then correct to use in (8.1) the incident and scattered wave vectors outside the pressure vessel [8.1].

The mechanism for inelastic light scattering can be viewed as a modulation of the dielectric susceptibility by some elementary excitation of the solid [8.2a]. The standard derivation leads to [8.2b, 3]

$$\frac{d^2\sigma}{d\Omega\, d\omega_s} = vV \frac{\omega_s^4}{c^4} |\hat{\varepsilon}_s \cdot \chi' \cdot \hat{\varepsilon}_i|^2 \langle UU^\dagger \rangle_\omega \tag{8.2}$$

for the differential cross section for scattering into the solid angle and frequency increments $d\Omega$ at Ω and $d\omega_s$ at ω_s.

Here χ' is the higher-order susceptibility tensor appropriate to the elementary excitation of amplitude U, $\hat{\varepsilon}_i$ and $\hat{\varepsilon}_s$ are the unit polarization vectors of incident and scattered light, v is the interaction volume and V is the sample volume. The notation $\langle UU^\dagger \rangle_\omega$ denotes the power spectrum of $|U|^2$.

Equation (8.2) is useful for our present purposes because it separates the cross section into a shape factor $\langle UU^\dagger \rangle_\omega$ which describes the frequency spectrum of the excitation under study, and a strength factor $|\hat{\varepsilon}_s \cdot \chi' \cdot \hat{\varepsilon}_i|^2$ which contains the relevant interactions of light with the elementary excitation through other possible intermediate excitations of the solid. To be more specific, for a one-phonon Stokes process we have [8.2b]

$$\langle UU^\dagger \rangle_\omega = \frac{\hbar}{2N\omega_i} (n_i + 1) g_i(\omega), \tag{8.3}$$

where N is the number of oscillators in the solid (note that $d^2\sigma/d\Omega\, d\omega_s$ actually depends on V/N not V), $n_i = [\exp(\hbar\omega_i/kT) - 1]^{-1}$ is the Bose thermal population factor and $g_i(\omega)$ is a line-shape response function, often taken to be a Lorentzian:

$$g_i(\omega) = \frac{\Gamma_i/2\pi}{(\omega_i - \omega)^2 + (\Gamma_i/2)^2}. \tag{8.4}$$

For a multiphonon process we must replace $(n_i + 1)$ in (8.3) by the appropriate thermal factor [e.g., $(n_1 + 1)(n_2 + 1)$ for a summation process involving ω_1 and ω_2]; $g_i(\omega)$ becomes the multiphonon density of states which generally contains several sharp critical point features [8.2b, 4, 5].

The vast majority of high pressure Raman measurements have been concerned with changes in the frequencies of lattice vibrations ω_i. These changes show up as spectral shifts of the peak of the Lorentzian, or the structure in the density of states. If the lifetime of the phonons is affected by pressure (e.g., through anharmonic interactions) then, in addition to spectral shifts, the observed line shape will also be modified. This occurs through changes in the full width of the Lorentzian Γ_i, or other appropriate width parameters.

The selection rules for Raman scattering are contained within the inner product $\hat{\varepsilon}_s \cdot \chi' \cdot \hat{\varepsilon}_l$ which selects specific components of the tensor χ' (often called the Raman tensor). The form of this (usually symmetric) tensor is determined by crystal symmetry [8.6, 7]. For a cubic solid of point group O_h, tensor components transforming as the irreducible representations Γ_1 (finite trace diagonal, also A_{1g}), Γ_{12} (traceless diagonal, also T_{2g}) and $\Gamma_{25'}$ (symmetric off diagonal, also E_g) appear. Only elementary excitations having wave functions transforming as these representations will be Raman active; they will contribute only to the tensor components associated with their representations. If compression causes a phase transition involving a change in point group symmetry, the Raman selection rules will also change. In general this is manifest through the appearance of new features in the observed spectra as forbidden excitations become Raman active and as degeneracies are lifted.

The magnitude of allowed Raman tensor components can also be affected by pressure without a phase transition. Consider one-phonon scattering in semiconductors. A typical two-band term contributing to $\hat{\varepsilon}_s \cdot \chi' \cdot \hat{\varepsilon}_l$ has the form [8.8]

$$\hat{\varepsilon}_s \cdot \chi' \cdot \hat{\varepsilon}_l \sim \frac{\langle v|\hat{\varepsilon}_s \cdot \boldsymbol{p}|c\rangle\langle c|H_{ep}^{(1)}|c\rangle\langle c|\boldsymbol{p} \cdot \hat{\varepsilon}_l|v\rangle}{(\omega_g + \omega_i - \omega_l)(\omega_g - \omega_l)}. \tag{8.5}$$

Equation (8.5) represents the process depicted in Fig. 8.2. Here $\boldsymbol{p}$ is the electron momentum, $H_{ep}^{(1)}$ is the relevant electron-phonon interaction and $|v\rangle$, $|c\rangle$, and ω_g are defined in Fig. 8.2.

Compression can modify either the matrix elements or the energy denominators in (8.5). Matrix element changes have not been studied in great detail; a

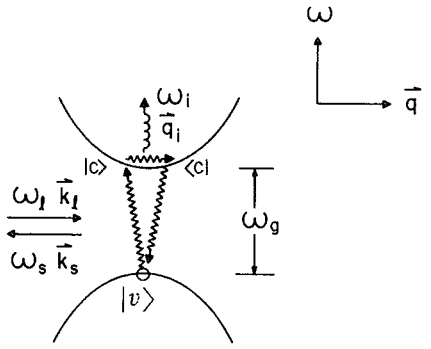

Fig. 8.2. A two-band process in which incident light ω_l, $\boldsymbol{k}_l$ excites an electron from the valence state $|v\rangle$ to the conduction state $|c\rangle$, the electron scatters to a different $\boldsymbol{q}$-state $\langle c|$ emitting a phonon ω_i, $\boldsymbol{q}_i$, and the electron recombines with the hole in $|v\rangle$ emitting scattered light ω_s, $\boldsymbol{k}_s$. The intermediate states $|c\rangle$ and $\langle c|$ should be summed over a complete set; ω_g is a $\boldsymbol{q} \approx 0$ direct bandgap

recent calculation estimates these effects to be too small for observation in Si [8.9]. In contrast, strong resonant Raman enhancement can be produced by pressure tuning the electronic gap ω_g through the zeros in the energy denominator at the incident and scattered frequencies.

To summarize, there are four principal pressure-Raman effects: these are frequency shifts of elementary excitations, line-shape changes, selection rule changes accompanying phase transitions and pressure-tuned resonant Raman scattering. We shall describe specific results that exemplify these categories, although space does not permit an exhaustive discussion in each case. Our main interest lies with covalent tetrahedral semiconductors and molecular solids. This is an important but partial subgroup of the extensive body of pressure-Raman studies. The reader is encouraged to refer to the several excellent reviews listed in the references for discussions of other solids [8.10–15].

8.1.2 Grüneisen Parameters and Scaling

Since much of our discussion will be concerned with pressure-induced phonon frequency shifts, a short discussion of Grüneisen parameters is appropriate.

The Grüneisen parameter γ_i for a quasi-harmonic mode i of frequency ω_i is defined by [8.16, 17]

$$\gamma_i = -\frac{\partial \ln \omega_i}{\partial \ln V} = \frac{1}{\beta}\frac{\partial \ln \omega_i}{\partial P}, \tag{8.6}$$

where β is the isothermal volume compressibility and the derivatives are evaluated at $P=0$. Essentially γ_i is an exponent that tells how ω_i *scales* with volume. Thus, if γ_i is independent of volume, (8.6) implies,

$$\frac{\omega_i(1)}{\omega_i(2)} = \left(\frac{V_2}{V_1}\right)^{\gamma_i}, \tag{8.7}$$

where $\omega_i(1)$ and $\omega_i(2)$ are the values of ω_i at volumes V_1 and V_2. The mode parameters γ_i are related to the macroscopic or average Grüneisen constant γ_{av} introduced by *Debye* [8.18] and *Grüneisen* [8.19] to discuss the equation of state of a solid. The Helmholtz free energy in the quasi-harmonic approximation is [8.20]

$$F = \Phi(V) + \Phi_D(T, V) - TS = \Phi(V) + \sum_i kT \ln[1 - \exp(-\hbar\omega_i/kT)], \tag{8.8}$$

where the $T=0$ internal energy $\Phi(V)$ is temperature independent and S is the entropy. In the Debye theory, $\Phi_D = Tf(\theta/T)$, where f is a universal function of θ/T with θ the Debye temperature. Using $-(\partial F/\partial V)_T = P$, we find the Debye equation of state

$$P = -\frac{\partial \Phi}{\partial V} + \gamma_{av}\frac{\Phi_D}{V}\left(\times \frac{\partial \ln \Phi_D}{\partial \ln\left(\frac{\theta}{T}\right)}\right) \tag{8.9}$$

where $\gamma_{av} = -(\partial \ln \theta / \partial \ln V)_T$. Employing the relation $-\partial^2 F/\partial V \partial T = \alpha/\beta$, where α is the volume thermal expansion, yields

$$\frac{V\alpha}{C_v \beta} = \gamma_{av} = \frac{\sum_i \gamma_i c_v(i)}{C_v}. \tag{8.10}$$

Here C_v is the crystal heat capacity and $c_v(i) = \partial(n_i \hbar\omega_i)/\partial T$ is the Einstein heat capacity for mode i. Grüneisen's approximation, viz. $\gamma_{av} = \gamma_{av}(V)$ independent of T, is justified for two situations (assuming that γ_i is T-independent): for $T \gg \theta$, we have $c_v(i) \approx k$ and $\gamma_{av} \approx (1/N) \sum_i \gamma_i$; for mode independent γ_i, (8.10) reduces to $\gamma_{av} = \gamma_i$ at any temperature.

The latter case applies to the Debye continuum limit for which $\gamma_i = \gamma_{av} = -\partial \ln \theta / \partial \ln V$. Since $\theta = (\hbar/k)\omega_D$ and $\omega_D = (cV/N)^{1/2} q_D$, where c is a characteristic (adiabatic) elastic constant and $q_D = 2\pi N/V^{1/3}$, we expect $\theta \propto c^{1/2} V^{1/6}$. This led *Slater* to propose [8.20]

$$\gamma_{av} = -\frac{1}{2}\left(\frac{\partial \ln B}{\partial \ln V}\right)_T - \frac{1}{6}, \tag{8.11}$$

where B is the adiabatic bulk modulus. Equation (8.11) and subsequent refinements have been employed by many authors [8.17, 21, 22].

We note in passing that γ_{av} is an important geophysical parameter. In the high-T and adiabatic limits, one obtains $T \propto V^{-\gamma_{av}}$. This equation of state is thought to apply to the earth's core [8.23].

8.2 Experimental Aspects

In recent years static high pressure techniques have become more accessible to non-specialists. Most relevant to the present chapter are the combined developments of the diamond-anvil press (Fig. 8.3) and the ruby calibration scale (Fig. 8.4) [8.24–26]. These developments have made practical and common, quantitative Raman measurements to several hundred kbar [8.27, 28]. Pressure-Raman techniques actually differ little from standard light scattering and high pressure procedures. Since there have been abundant individual discussions of these, we shall not dwell at length on this subject (see, for example, [Ref. 8.3, Chap. 2], [Ref. 8.14, Chap. 4], and [8.29–8.33b]). Instead we wish to discuss several operational problems common to most pressure-Raman work.

A difficulty often encountered is a large background that overwhelms the Raman signal. This holds for most common apparatus, such as the diamond-anvil press (Fig. 8.3), the NaCl press [8.32], the oil bomb [8.29] and variations on these (the problem is less for a gas bomb [8.34]). The background can be due to direct and specular reflections, elastic and inelastic scattering, and fluorescence, from the cell windows, packing, walls, the pressure transmitting medium and the sample.

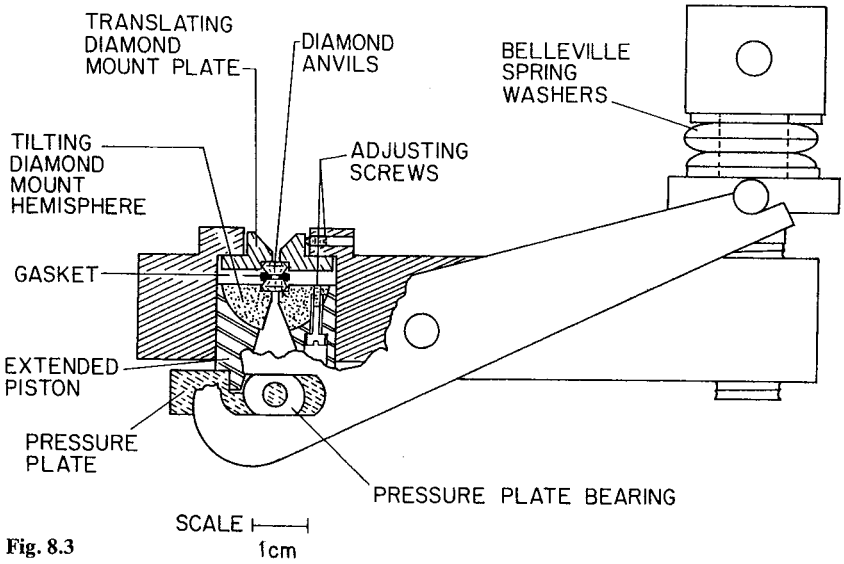

Fig. 8.3

Fig. 8.3. Cutaway cross-section drawing showing the essential parts of the modern diamond-anvil cell developed by the National Bureau of Standards (U.S.) group. Under proper operation, several hundred kbar can be routinely achieved without disturbing optical access. After [8.24]

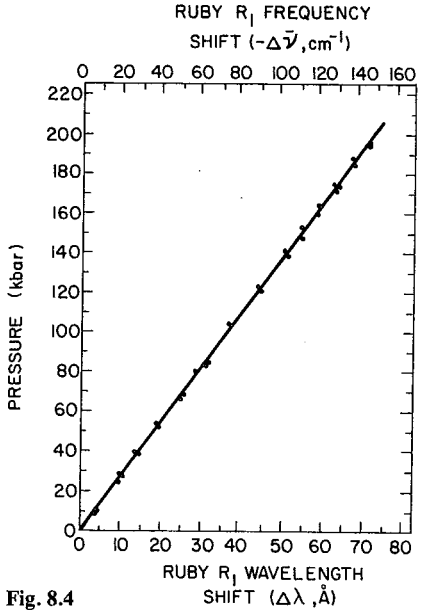

Fig. 8.4

Fig. 8.4. Original calibration for the ruby secondary pressure scale. The R_1 fluorescence line (6942 Å at $P=0$, $T=298$ K) shifts by 0.365 Å/kbar. After [8.26]

Techniques to limit the background include [8.27] varying the laser frequency away from fluorescence bands, sharp cut filters, crossed polarizers in the incident and scattered beams, triple monochromators, spatial discrimination by aperture stops and temporal discrimination (against slow fluorescence) by pulsed techniques. Right-angle scattering is always preferable, but not always

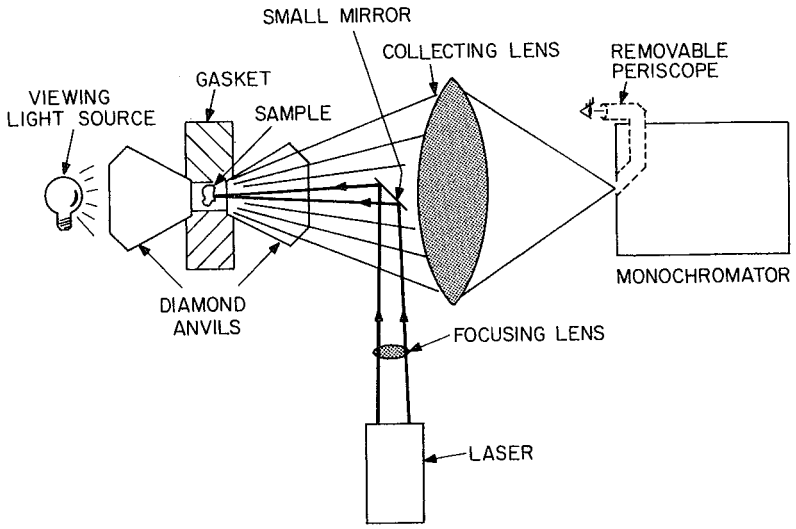

Fig. 8.5. A Raman experiment using the diamond cell in the back-scattering geometry. This schematic drawing is not to scale. After [8.27]

possible, as for opaque samples or the diamond-anvil press. In such cases the back-scattering geometry (generally superior to forward scattering) should be used; Fig. 8.5 shows a typical arrangement. As a rule of thumb for the diamond-cell, one should not expect to observe a signal of <100 counts/s below a Raman shift of 50 cm^{-1}.

A secondary concern is a reduced signal due to the small (often microscopic) sample size required by many apparatus to reach high pressure. The ability to tightly focus (≤ 30 μm inside the pressure chamber) modern coherent sources generally minimizes this problem. However, one must take care not to exceed sample damage thresholds (the standard technique of focussing with a cylindrical lens cannot be used). For the diamond cell, it is typical to find signal reductions of only $1/2-2/3$ below levels measured outside the cell [8.27]. When working with small specimens, some means for visually observing the sample during alignment is a great advantage.

The ruby fluorescence (R_1 and R_2-lines) pressure scale (Fig. 8.4) developed by the U. S. National Bureau of Standards group [8.24, 26] has become a widely accepted secondary standard with $\sim 3\%$ accuracy. Subsequent work showed that the expression $P(\text{Mbar}) = 3.808\,[(\lambda/\lambda_0)^5 - 1]$, where $\lambda_0 = 6942$ Å and λ are the R_1 wavelengths at $P=0$ and $P>0$ ($T=300$K), respectively, could be used into the megabar regime [8.33a]. The R_1-scale was also extended to low temperature [8.35]. The ruby fluorescence technique is ideal for Raman experiments because the internal cell pressure can be quickly determined without changing the measuring equipment or geometry (the laser wavelength must be shorter than λ_0). Sometimes it is advantageous to calibrate the strongest Raman line, in an

otherwise weak spectrum, against R_1, and then to measure the entire spectrum in a separate loading without ruby, thereby eliminating the ruby luminescence from the background [8.27].

8.3 Phonon Frequencies Under Pressure in Tetrahedral Semiconductors

Here we discuss the effects of compression on the entire phonon dispersion of several prototype materials. This has become possible through a combination of one and two-phonon Raman measurements, and our account is so divided. The reader should refer often to Tables 8.1 – 3 which extend the discussion to other solids and give detailed references.

8.3.1 One-Phonon Spectra and the Transverse Effective Charge

The diamond and zincblende structures can be viewed as two interpenetrating fcc sublattices, separated by 1/4 of a cube body diagonal along (111). The $\boldsymbol{q}=0$ (Γ-point) groups are O_h and T_d, respectively, with two identical atoms per primitive cell in the former and one cation-anion pair in the latter. This leads to three acoustic and three optic modes. Because the diamond structure has inversion symmetry the optic modes are degenerate (no LO-TO splitting); they transform as $\Gamma_{25'}$ (E_g) making them Raman active but infrared (ir) inactive. There will be just one first-order Raman peak, hereafter designated $O(\Gamma)$. The heteropolar zincblende materials do not possess inversion symmetry, so that longitudinal LO(Γ) and transverse TO(Γ) phonons are not degenerate. Instead we have [8.2b, 36]

$$\omega_{\mathrm{LO}}^2-\omega_{\mathrm{TO}}^2=\frac{4\pi N_{\mathrm{d}}e^{*2}}{\varepsilon_\infty \mu V}=\omega_{\mathrm{TO}}^2\,\frac{(\varepsilon_0-\varepsilon_\infty)}{\varepsilon_\infty}, \tag{8.12}$$

which defines Born's transverse dynamic effective charge e^*. Here N_{d}/V is the density of cation-anion dipole pairs, ε_∞ and ε_0 are the optical and static dielectric constants, and μ is the reduced mass. The middle expression defines the plasma frequency of the ions squared, and the far right-hand side makes explicit use of the Lyddane-Sachs-Teller relation $\omega_{\mathrm{LO}}^2/\omega_{\mathrm{TO}}^2=\varepsilon_0/\varepsilon_\infty$. The modes have Γ_{15} (E) symmetry; they are Raman and ir active. There will be two first-order Raman peaks corresponding to TO(Γ) and LO(Γ).

The effect of hydrostatic pressure to 125 kbar on $O(\Gamma)$ in Si is displayed in Fig. 8.6 after [8.27]. These high pressure results agree with earlier measurements by *Buchenauer* et al. [8.37] to 9 kbar. The Raman peak shifts to higher energy by about 25 cm^{-1} in 100 kbar without changing shape. This corresponds to $\gamma_{O(\Gamma)}=0.98\pm0.06$, nearly equal to unity. $\gamma_{O(\Gamma)}\approx 1.0$ is a general characteristic of covalent group IV semiconductors, and may be viewed as a norm for

Table 8.1. Glossary of Grüneisen parameters for tetrahedral semiconductors measured by pressure-Raman scattering (except for $q=0$ acoustic modes[a]). Branches (in order of descending energy) and critical points are arranged to match usual phonon dispersion format [8.51]. Best values are listed; in most cases uncertainty occurs in last decimal place

Branch	Material	Critical points				Material	Critical points				Material	Critical points			
		X	*K*	*Γ*	*L*		*X*	*K*	*Γ*	*L*		*X*	*K*	*Γ*	*L*
LO	C[1-4]	1.3		1.19	1.27	GaAs[8,12,18,19,20]			1.23		ZnTe[3,22,23,27,28]	1.7		1.2	1.8
TO(2)		2.0		1.19	1.4		1.73		1.39	1.5		1.8		1.7	
TO(1)		2.0		1.19	1.4		1.73		1.39	1.5		1.8		1.7	
LA				1.06[a]					1.3[a]					1.55[a]	
TA(2)		0.4[b]		0.97[a]			−1.62	−0.4	0.53[a]	−1.7		−1.55	−0.4	0.20[a]	−1.0
TA(1)		0.4[b]	0.4[b]	0.51[a]			−1.62	−1.62	−0.05[a]	−1.7		−1.55	−1.55	−0.43[a]	−1.0
LO	Si[5-10]	0.9[c]	0.9[c]	0.98	0.9[c]	GaSb[8,12,21]			1.21		CuCl[29-33]			1.0[e]	
TO(2)		1.5		0.98	1.3				1.23					2.4[e]	
TO(1)		1.5	1.5	0.98	1.3				1.23					2.4[e]	
LA		0.9[c]	0.9[c]	1.1[a]	0.9[c]				1.4[a]					1.45[a]	
TA(2)		−1.4	−0.3	0.33[a]	−1.3				0.48[a]			−1.4[f]		−0.39[a]	−1.4[f]
TA(1)		−1.4	−1.0	−0.05[a]	−1.3				−0.004[a]			−1.4[f]	−1.4[f]	−1.87[a]	−1.4[f]
LO	Ge[6,8,9,11,12]			1.12		InP[18]			1.24		CuBr[30,31,33]			1.9[e]	
TO(2)				1.12			1.4		1.44	1.4				2.4[e]	
TO(1)				1.12			1.4		1.44	1.4				2.4[e]	
LA				1.3[a]											
TA(2)		−1.53		0.62[a]			−2.1	−0.3		−2.0		−0.4[f]			−0.4[f]
TA(1)		−1.53		0.17[a]			−2.1	−2.1		−2.0		−0.4[f]	−0.4[f]		−0.4[f]
LO	AlSb[8]			1.27		ZnS[3,22-26]	1.1		0.95	1.1	CuI[30,31,33,34]			1.6[e]	
TO(2)				1.23			1.0			1.0				2.2[e]	
TO(1)				1.23			1.0			1.0				2.2[e]	
LA									1.34[a]						
TA(2)							−1.2	−0.3	0.21[a]	−1.5		2.5			2.5
TA(1)							−1.2	−1.2	−0.90[a]	−1.5		2.5	2.5		2.5

Table 8.1 (continued)

Branch	Material	Critical points				Material	Critical points			
		X	K	Γ	L		X	K	Γ	L
LO	GaP[3,5,13–17]		1.27	0.95		ZnSe[3,12,22,23,27]	0.9		0.9	0.9
TO(2)		1.3		1.09	1.50		1.6		1.4	1.6
TO(1)		1.3		1.09	1.50		1.6		1.4	1.6
LA		1.0[d]	1.0[d]	1.4[a]			1.1		1.45[a]	1.1
TA(2)		−0.72	0.15	0.49[a]	−0.81		−1.3	−0.4	0.16[a]	−1.5
TA(1)		−0.72	−0.72	−0.2[a]	−0.81		−1.3	−1.3	−0.60[a]	−1.5

[a] From measurements of the elastic constants c_{11}, c_{44}, $(c_{11}-c_{12})/2$ corresponding, respectively, to LA, TA(2), TA(1)
[b] Calculated using optic mode data and a Born-von Karman model
[c] From fitting the temperature dependent thermal expansion
[d] From the line-shape study of [8.78]
[e] Measured at 40K
[f] From measurements on $CuCl_{0.80}$ $Br_{0.20}$ and $CuCl_{0.20}$ $Br_{0.80}$

1 [8.39]
2 H. J. McSkimin, P. Andreatch, Jr.: J. Appl. Phys. **43**, 2944 (1972)
3 [8.38]
4 M. H.Grimsditch, E. Anastassakis, M. Cardona: Phys. Rev. B**18**, 901 (1978)
5 [8.27]
6 H. J. McSkimin, P. Andreatch, Jr.: J. Appl. Phys. **35**, 3312 (1964)
7 [8.52]
8 [8.37]
9 J. B. Renucci, M. A. Renucci, M. Cardona: Solid State Commun. **9**, 1651 (1971)
10 E. Anastassakis, A. Pinczuk, E. Burstein: Solid State Commun. **8**, 133 (1970)
11 [8.96]; see this reference also for results on 3*C*-SiC
12 F. Cerdeira, C. J. Buchenauer, F. H. Pollak, M. Cardona: Phys. Rev. B**5**, 580 (1972)
13 [8.41]
14 [8.53]
15 [8.60]
16 [8.78]
17 I. Balslev: Phys. Stat. Solidi (b) **61**, 207 (1974)
18 [8.42a]
19 H. J. McSkimin, A. Jayaraman, P. Andreatch, Jr.: J. Appl. Phys. **38**, 2362 (1967)
20 [8.97]
21 H. J. McSkimin, P. Andreatch, Jr., T. B. Bateman: J. Appl. Phys. **39**, 4127 (1968)
22 [8.54]
23 [8.43a]
24 [8.88]
25 E. Chang, G. R. Barsch: J. Phys. Chem. Sol. **34**, 1543 (1973)
26 [8.55]
27 B. H. Lee: J. Appl. Phys. **41**, 2988 (1970)
28 [8.61]
29 R. C. Hanson, K. Helliwell, C. Schwab: Phys. Rev. B**9**, 2649 (1974)
30 [8.59]
31 H. D. Hochheimer, M. L. Shand, J. E. Potts, R. C. Hanson, C. T. Walker: Phys. Rev. B**14**, 4630 (1976)
32 [8.83]
33 [8.84a]
34 [8.58]

Table 8.2. Supplementary listing of mode γ's for tetrahedral and related solids measured by various techniques

Material	Critical point (diamond, zb) mode γ's				
Ge(diam.)[a], tunneling	TA(L)	LA(L)	TO(L)	LO(L)	
1.2 K, uniaxial	−0.4	0.5	0.9	1.2	
ZnS(wurt.)[b,c],	TA($X;K$)	TO(Γ)	LO(Γ)	TO($X;L$)	LO($X;L$)
Raman	(2nd order)	(A_1, E_1)	(A_1, E_1)	(2nd order)	(2nd order)
hydrostatic	−1.8	1.8	1.0	1.3	1.4
		2.0[c]			
ZnO(wurt.)[c,d],	TA(L)	TO(L)	TO(Γ)		
Raman	(E_2)	(E_2)	(A_1)		
hydrostatic	−1.8	1.7	2.1		
CdS(wurt.)[c−e],	TA(L)	TO(L)	TO(Γ)	LO(Γ)	
Raman	(E_2)	(E_2)	(E_1) (A_1)	(E_1) (A_1)	
hydrostatic,	−2.7[c,d]			1.1[d]	
uniaxial 77 K	−2.2	1.6	1.0 1.8	0.8* 1.4*	
CuI(rhom., tetrag.)[f]	TA(L)	LA(L)	TO(Γ,L)	[TA(X) LA(X) TO(Γ,X)	
Raman	(E)	(A_1)	(E)	(E_g) (A_{1g}) (E_g)]	
hydrostatic	3.2	1.6	1.5	>0	
AgI(wurt.)[g]	TA(L)	InAs(zb)[h]		TO(Γ)	
Raman	(E_2)	Raman			
hydrostatic	−7.5	uniaxial		0.9	

* In e (below) the LO−TO splitting is assumed pressure independent

[a] R. T. Payne: Phys. Rev. Lett. **13**, 53 (1964) [b] [8.88] [c] [8.43a] [d] [8.38]
[e] R. J. Briggs, A. K. Ramdas: Phys. Rev. **B13**, 5518 (1976) [f] [8.58] [g] [8.89]
[h] F. Cerdeira, C. J. Buchenauer, F. H. Pollak, M. Cardona: Phys. Rev. **B5**, 580 (1972)

comparison. The measured $\gamma_{O(\Gamma)}$ values for diamond [8.38, 39] and Ge [8.37, 40] are within 20% of unity (see Table 8.1). Thus, for the strictly covalent materials $\omega_{O(\Gamma)}$ scales as V^{-1}, and the corresponding force constants scale quadratically with density.

This situation changes for the partially ionic zincblende materials. Typical data for the TO(Γ) and LO(Γ) Raman peaks of GaP [8.41] and InP [8.42a] are shown in Figs. 8.7, 8, and the measured results for other materials are summarized in Tables 8.1, 2. *Mitra* et al. [8.38, 43a] studied several of the tetrahedral solids in Tables 8.1, 2, as well as some alkali halides. They found that $\gamma_{LO(\Gamma)}$ maintains an approximately constant value close to one, but that $\gamma_{TO(\Gamma)}$ increases above unity with increasing effective charge. This correlation is demonstrated in Fig. 8.9, where $\gamma_{TO(\Gamma)}$ is plotted against the Szigetti effective charge per cation valence electron e_s^*/ze. Here $e_s^* = 3e^*/(\varepsilon_\infty + 2)$, where the factor $3/(\varepsilon_\infty + 2)$ corrects for the local field due to ion polarizability. *Mitra* and *Namioshi* [8.43b] considered several models to explain their data including a Born-Mayer treatment for the alkali halides, and the Phillips ionicity theory for

Table 8.3.† Effect of compression on Born's effective charge expressed as γ_{e^*}, and parameters necessary to compute γ_{e^*} from (8.13)

Material	ε_∞[a]	$\gamma_{\varepsilon_\infty}$[b]	ν_{TO}[c] [cm^{-1}]	ν_{LO}[c] [cm^{-1}]	γ_{TO}	γ_{LO}	γ_{e^*}
AlSb	10.2	−1.0	319	340	1.23	1.27	0.6
GaP	9.1	−0.6	367	403	1.09	0.95	−0.5
GaAs	10.9	−0.8	269	292	1.39	1.23	−0.5
GaSb	14.4	−1.3	231	241	1.23	1.21	−0.1
InP	9.6	−0.8	304	345	1.44	1.24	−0.3
ZnS	5.2	−0.2	271	352	1.9*	0.95	−1.0
ZnSe	5.9	−0.3	205	250	1.4	0.9	−0.8
ZnTe	7.3	−0.6	177	205	1.7	1.2	−1.0
CuCl	3.7	0.0	158[d]	210[d]	2.4	1.0	−1.3
CuBr	4.4	−0.2	135[d]	170[d]	2.4	1.9	0.5
CuI	5.5	−0.4	133[d]	151[d]	2.2	1.6	−1.1

† See text and [8.42b] for very recent results on 3*C*-SiC, AlN, BN, and BP

* The average of both values in Table 8.2 for the E_1/A_1 TO(Γ) modes in wurtzite ZnS

[a] [8.48]

[b] [8.45]; $\gamma_{\varepsilon_\infty}$ was calculated from the best fit line with slope −3.8 eV [Ref. 8.45, Fig. 4] using $E_g=[(C^2+E_h^2)2/3]^{1/2}$ from [8.48]

[c] W. Richter: "*Resonant Raman Scattering in Semiconductors*", in Springer Tracts Mod. Phys. **78**, 174 (1976)

[d] H. D. Hochheimer, M. L. Shand, J. E. Potts, R. C. Hanson, C. T. Walker: Phys. Rev. B**14**, 4630 (1976); data recorded at 40K

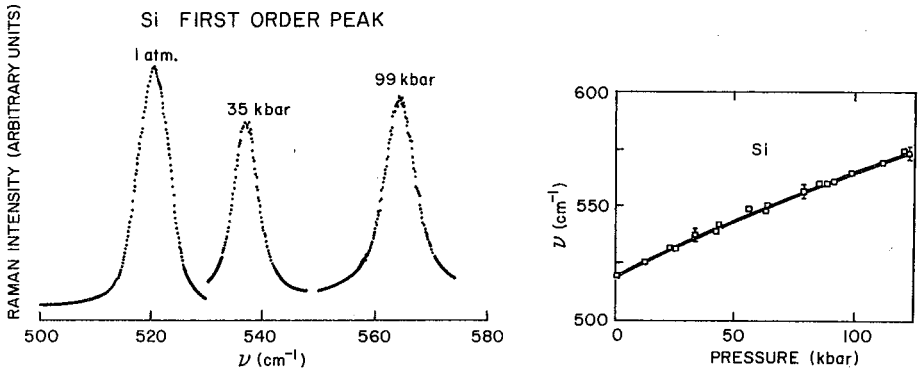

Fig. 8.6. Shift to higher frequency with pressure (300 K) of the first-order Raman peak of Si. In the right-hand plot the initial $P=0$ slope gives $\gamma_{O(\Gamma)}\approx 1$ for this prototypical homopolar semiconductor. After [8.27]

the more covalent semiconductors [8.48]. In the latter approach the homopolar gap was taken to scale as $V^{-2/3}$ and the bond ionicity to be proportional to e_s^{*2}. Both treatments predicted a decrease in e_s^* with pressure.

These experimental and theoretical findings show that compression tends to reduce the effective charge for a considerable sampling of different ionicity materials. However zincblende-type 3*C*—SiC is an exception (see below and

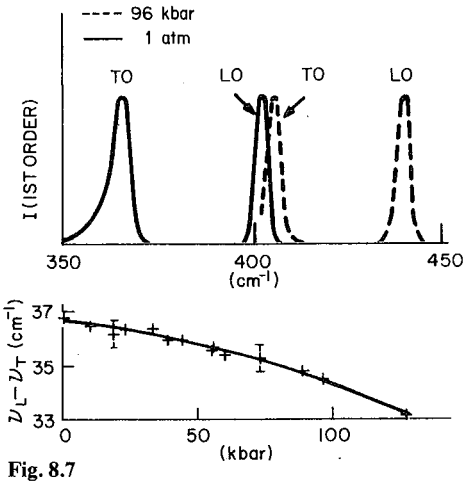

Fig. 8.7

Fig. 8.7. Shift with pressure (300 K) of the first-order TO and LO phonon peaks of GaP [8.41]. The LO − TO splitting decreases under compression as shown in the lower plot

Fig. 8.8. Shift with pressure (300 K) of the first-order TO and LO phonon peaks of InP. In the right-hand plot, phonon frequency is shown versus lattice constant (*linear lower scale*) and pressure (*upper scale*). After [8.42a]

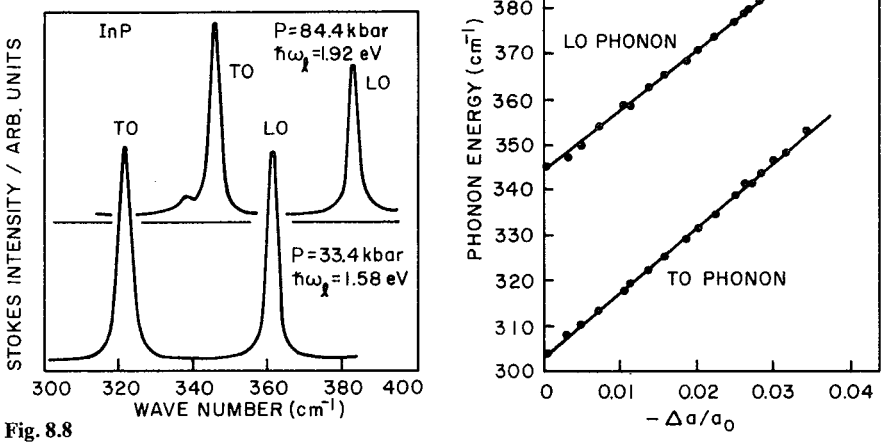

Fig. 8.8

[8.42b]). From (8.12), the Grüneisen parameter γ_{e^*} for Born's dynamic charge is given by

$$\gamma_{e^*} = -\frac{1}{2} + \frac{1}{2}\gamma_{\varepsilon_\infty} + \gamma_{\mathrm{LO}} + (\gamma_{\mathrm{LO}} - \gamma_{\mathrm{TO}})\frac{\varepsilon_\infty}{\varepsilon_0 - \varepsilon_\infty}. \tag{8.13}$$

Values of γ_{e^*} calculated using (8.13) are listed in Table 8.3 for several III-V, II-VI and I-VII solids.

Recently, *Trommer* et al. [8.42a, 44] studied in detail the volume dependence of e^* for GaAs and InP. They found $e^*/e = 2.18 + 4.4(\Delta r/r_0) - 88(\Delta r/r_0)^2$ and $e^*/e = 2.54 + 4.5(\Delta r/r_0) - 88(\Delta r/r_0)^2$ for GaAs and InP, respectively; here r is the nearest-neighbor separation. Thus, $\gamma_{e^*} \approx -2/3$ for both materials with a non-negligible quadratic contribution. The variations of γ_{e^*}, obtained in this way,

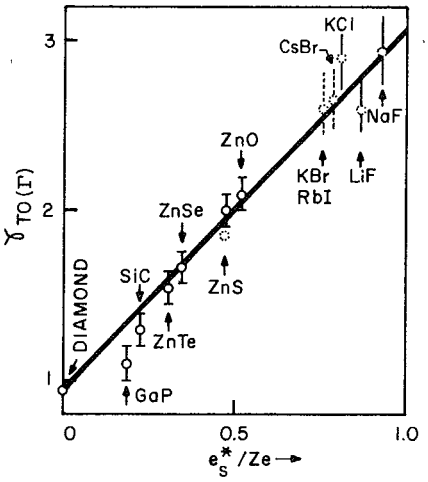

Fig. 8.9. Linear relationship between the Grüneisen parameter for TO(Γ) and the Szigetti effective charge per cation electron discovered by *Mitra* et al. [8.38, 43a]. Closed circles Raman data, open circles ir data

from the values listed in Table 8.3 for GaAs and InP, stem from using (8.13) in Table 8.3 and from the means of estimating $\gamma_{\varepsilon_\infty}$. In [8.42a, 44], $\gamma_{\varepsilon_\infty} = -1$, whereas in Table 8.3, $\gamma_{\varepsilon_\infty}$ was estimated according to the correlations established in [8.45].

To explain their pressure-Raman data on GaAs and InP, *Trommer* et al. applied two theoretical approaches appropriate for the e^* of partially covalent semiconductors. These are the bond orbital model (BOM) of *Harrison* and *Ciraci* [8.46] and the dielectric matrix pseudopotential (DMP) method of *Vogl* [8.47].

In the BOM e^* is given by

$$e^* = -\Delta z e + 4\alpha_p e + 4c\alpha_p(1-\alpha_p^2)e, \tag{8.14}$$

where $-\Delta z e = \frac{1}{2}(z_{\text{anion}} - z_{\text{cation}})e$ is the charge due to equal covalent sharing of the valence electrons, $c \approx 1$ is an adjustable parameter and α_p is the bond polarity giving the amount of asymmetric charge transfer. Note that both static ($4\alpha_p e$) and dynamic [$4c\alpha_p(1-\alpha_p^2)e$] terms must be included. α_p is defined by the covalent and polar energies W_2 and W_3 [8.46], which are similar to E_h and C in the theory of *Phillips* and *Van Vechten* [8.48]:

$$\alpha_p = \frac{W_3}{(W_2^2 + W_3^2)^{1/2}}. \tag{8.15}$$

W_2 is known to scale as $V^{-n/3}$ with $n \approx (2.0-2.5)$, and W_3 is thought to depend weakly on volume. Accordingly, under compression α_p decreases, and since for the materials of interest $8\alpha_p > \Delta z$, e^* also decreases. Neglecting the term in α_p^3 we have $\gamma_{e^*} \approx \gamma_{\alpha_p}$, and for small W_3 (strongly covalent solids) $\gamma_{e^*} \approx -2/3$, in agreement with the measurements of [8.42a, 44] for InP and GaAs. However, this simple approach cannot explain the nonlinear dependence of e^* on $\Delta r/r_0$.

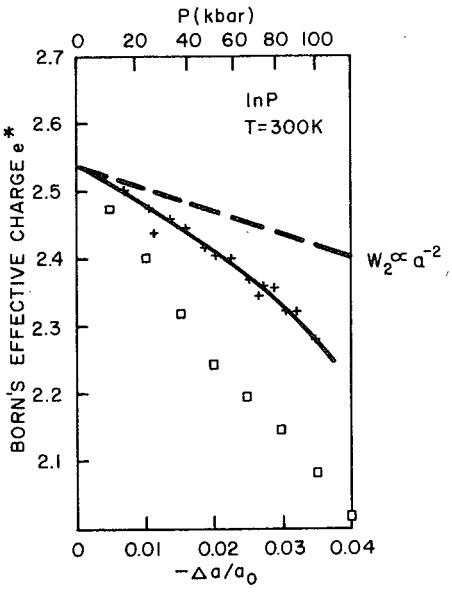

Fig. 8.10. Effective charge e^* versus lattice constant and pressure for InP. *Crosses* and *solid line* are data and fit; *dashed line* and *squares* are the results of BOM and full DMP calculations, respectively (see text). After [8.42a]

In the DMP method of *Vogl* an expression for e^* [Ref. 8.42a, Eq. (10)] is obtained by calculating the sublattice-displacement induced change in charge density using pseudopotential techniques. Care must be taken to maintain self-consistency. In the simplest Heine-Jones type band structure [8.49], an expression is obtained which is approximately equivalent to (8.15) for $\alpha_p^2 \leq 0.6$ (valid for groups III – V and II – VI). W_2 and W_3, determined only by the (111) form factors in this approximation, are expected to scale with volume as before [8.46,48]. Thus the DMP method can also explain $\gamma_{e^*} \approx -2/3$.

For InP in Fig 8.10, the result of an extensive DMP calculation (squares), including form factors with $|\boldsymbol{G}| \leq (2\pi/a_0)\sqrt{11}$ ($\boldsymbol{G}$ and a_0 are a reciprocal lattice vector, and the lattice constant), is compared with experiment (crosses) and the BOM (dashed line). The extensive DMP result overestimates, and the BOM underestimates the effect by the same amount. Nevertheless, the sign and magnitude of the change are successfully reproduced, showing that both models contain the essential physics. Very recently the work of this group has been extended [8.42b]. Pressure-Raman measurements on 3*C*-SiC, AlN, BN, and BP gave for γ_{e^*} +0.67, −0.65, −0.17, −2.49, respectively, and DMP calculations yielded qualitative agreement for γ_{e^*}, reproducing the correct sign in each case. The increase in e^* with pressure for 3*C*-SiC was attributed to the lack of *p*-electrons in the carbon core.

A density functional pseudopotential (DFP) calculation of e^* in GaAs was also reported recently [8.50]. This method is well suited to pressure effects because it is not restricted to small displacements. It will be discussed further in Sects. 8.3.4, 5.2.

8.3.2 Phonon Dispersion at High Pressure – Two-Phonon Results

For the tetrahedral semiconductors, the interpretation of two-phonon pressure-Raman data is generally aided by the resemblance of the dominant Γ_1-component to the density of phonon overtone states [8.4,5]. This is just the single-phonon density on a doubled frequency scale. For example, compare the Raman spectra and density of states for Ge in Fig. 8.11. For III – V and II – VI materials, the similarity continues for the TA modes, but lessens for the optic modes (see Figs. 8.13, 14 and [8.51] for GaP and ZnS). This fortunate circumstance arises because the matrix elements in $\hat{\varepsilon}_s \cdot \chi' \cdot \hat{\varepsilon}_l$ [see (8.2,5)] do not strongly modulate the density obtained by integrating (8.4) over the kinematically allowed phonon states. Since, in addition, the crystal symmetry is invariant under hydrostatic conditions, it is possible to monitor the entire phonon dispersion under pressure. Examples will be given below. The prototypical materials Si, GaP, and ZnS will be discussed in detail; data for other solids are presented in Tables 8.1, 2. The known homologies at $P=0$ can often be used to extend these results to solids where less detailed pressure data exist.

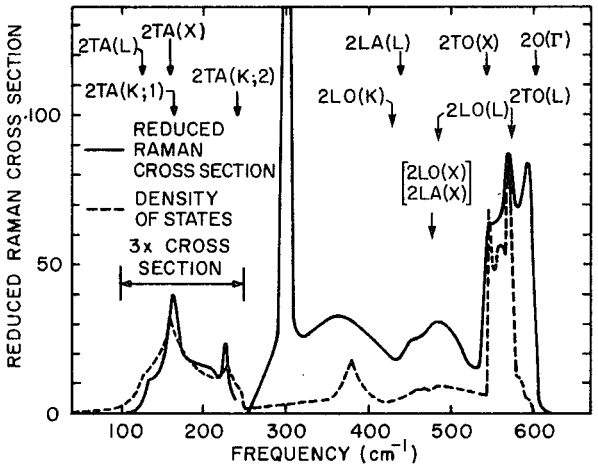

Fig. 8.11. Reduced [divided by $(n_i+1)^2$] $\Gamma_1+4\Gamma_{12}$ component of the two-phonon Raman spectrum of Ge ($P=0$, $T=300$ K) compared with the density of overtone states from neutron scattering. Note close similarity in 2TA region. Critical point designations match those in Tables 8.1,2. After [8.4]

The two-phonon spectra of Si and GaP were studied by *Weinstein* and *Piermarini* [8.27, 41] in the first use of the modern (Ruby-calibrated, hydrostatic) diamond cell for Raman measurements. Lower pressure (≤ 10 kbar) measurements were reported for Si by *Richter* et al. [8.52] and for GaP by *Weinstein* et al. [8.53]. Second-order scattering in cubic ZnS was investigated to 150 kbar by *Weinstein* [8.54] and at lower pressure by *Brafman* and *Mitra* [8.43] and *Zigone* et al. [8.55]. Data from [8.27, 41, 54] are reproduced in Figs. 8.12 – 14. The critical point designations match those in Tables 8.1, 2 and in the phonon dispersion curves, Figs. 8.15 – 17. Note that the peaks and shoulders in the spectra are derived from a collection of modes in the vicinity of a critical point. For example, the strongest peak in the TA overtone spectrum is due to a large set of nearly degenerate phonons extending over the Brillouin zone (BZ) surface

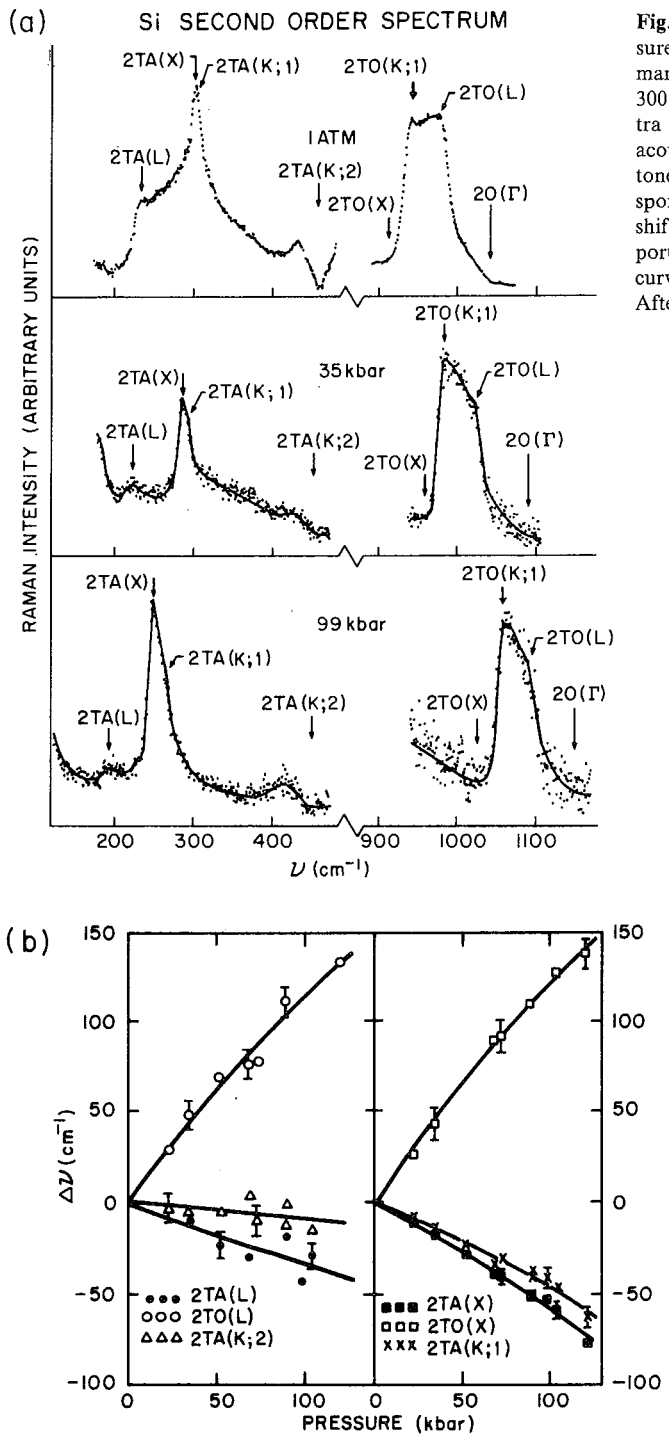

Fig. 8.12a,b. Effect of pressure on the two-phonon Raman spectrum of Si (at 300 K). **(a)** Measured spectra in the regions of strong acoustical and optical overtone scattering. **(b)** Corresponding plots of frequency shift versus pressure for important critical points. Solid curves are least-square fits. After [8.27]

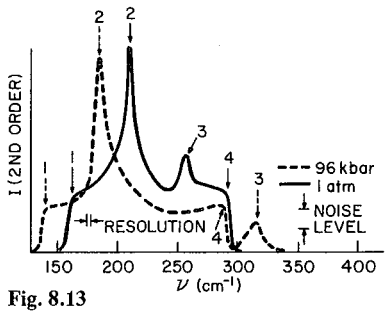

Fig. 8.13

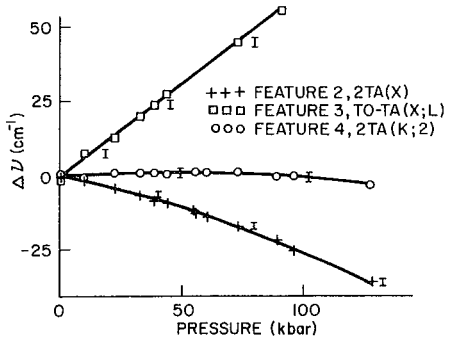

Fig. 8.13. Raman spectrum of GaP (300 K) in the 2TA region as a function of pressure. The right-hand figure plots frequency shift versus pressure for important critical points; error bars are displaced from best fit curves. After [8.41]

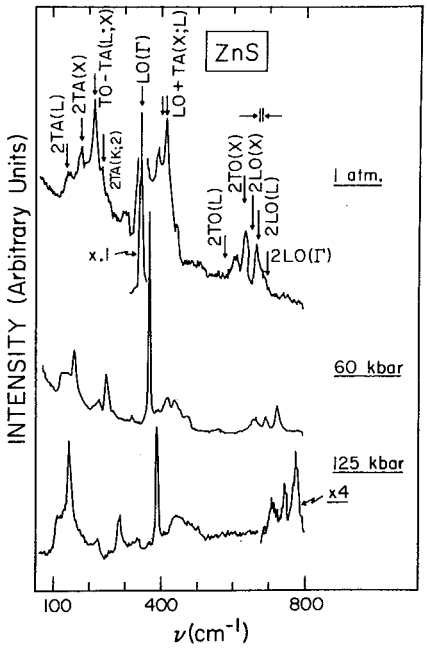

Fig. 8.14

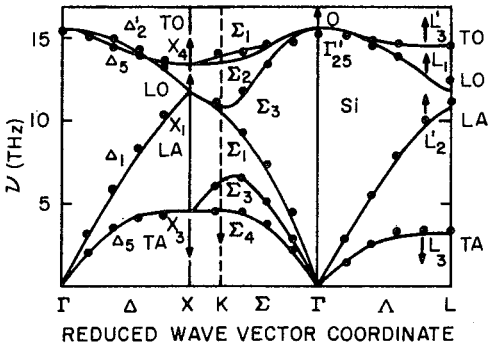

Fig. 8.15

Fig. 8.14. Effect of pressure on the Raman spectrum of cubic ZnS at 300 K. After [8.54]

Fig. 8.15. Phonon dispersion relations for Si ($P=0$, $T=300$ K) measured by neutron scattering (*points*) and fit to a model calculation (*curves*). Band labels and irreducible representations are indicated. *Arrows show direction of pressure response* (see [8.51] and references therein)

from X to K and into the zone by $\sim 1/3$ the distance to Γ along the Σ and Δ-directions.

The pressure results for Si, GaP, and ZnS are as follows. The BZ center optical phonons have already been discussed. Proceeding on the LO branch along the (00ζ) and $(\zeta\zeta\zeta)$ directions to the BZ boundary X and L-points, the mode Grüneisen parameters change little. There is only a $15-20\%$ increase in γ_i for GaP and ZnS (no BZ boundary LO data exist for Si). For the TO branches of

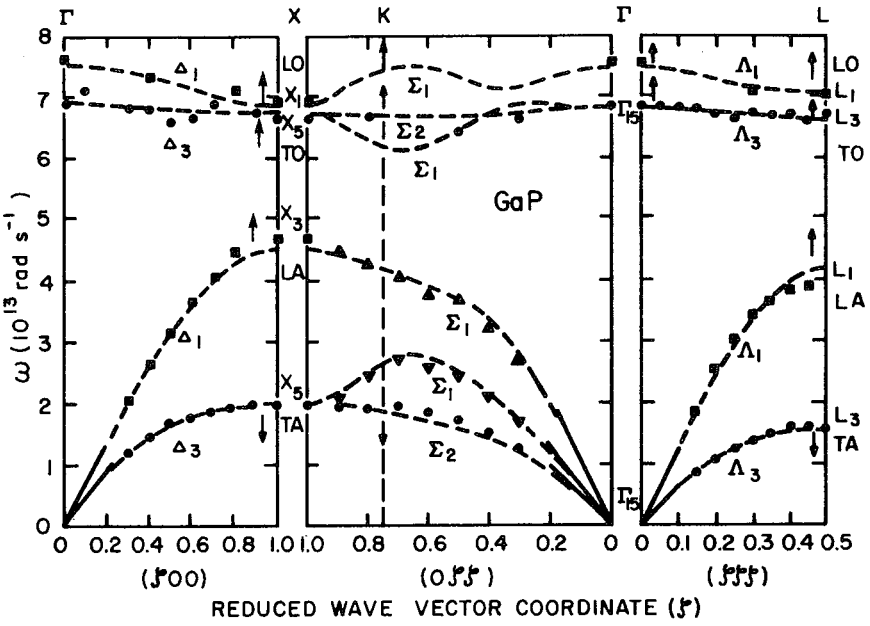

Fig. 8.16. Phonon dispersion relations for GaP. Key same as in Fig. 8.15

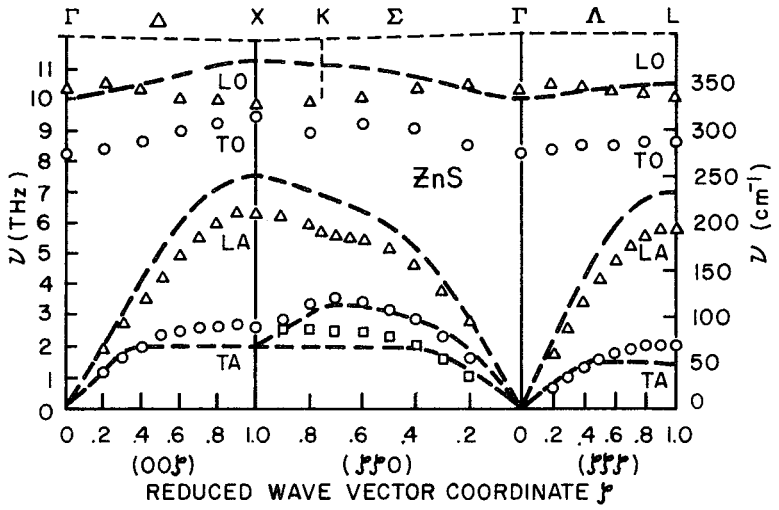

Fig. 8.17. Phonon dispersion relations (300 K) for ZnS at $P=0$ measured by neutron scattering (*points*), and at $P=150$ kbar deduced from pressure-Raman studies at critical points (*dashed curves*). 150 kbar marks onset of the metallization transition. See Sect. 8.5.2. After [8.54]

Si and GaP, γ_i also increases slightly away from $\boldsymbol{q}=0$ reaching ~ 1.4 at the X and L-points, but for ZnS the reverse is true. For each material the initial effect of pressure is to further flatten the already Einstein-like LO and TO branches [8.54]. However, one should be careful not to generalize this result to other solids until more data is collected. No pattern emerges as to whether pressure causes the LO and TO branches to cross or separate. For GaP, $\gamma_{TO(L)} > \gamma_{LO(L)}$ implying eventual crossing at the L-point, while for ZnS the situation is ambiguous (Tables 8.1, 2). The lack of a pattern is consistent with the $P=0$ dispersion curves for which LO and TO may (as in GaAs) or may not (as in GaP) cross [8.51]. No data exist to distinguish the pressure behavior of the two nondegenerate TO branches along low-symmetry directions.

Consider now the acoustic branches. There are no direct pressure data for BZ boundary LA modes, as these do not appear strongly in the two-phonon Raman spectra, and they are often dominated by nearby first-order peaks (see the densities of states in [8.51]). However, in group IV materials, LO(X) and LA(X) are degenerate by symmetry, and they remain close for many tetrahedral semiconductors at both the X and L-points (again see, for example, GaAs, InSb, ZnSe, and CdTe [8.51]). Consequently we take $\gamma_{LA} \approx \gamma_{LO}$ at the BZ boundary as a zeroth-order approximation. This is supported by recent calculations for ZnS, ZnSe, and ZnTe showing that γ_{LA}, γ_{LO} (and also γ_{TO}) change little across the BZ [8.56]. For Si, $\gamma_{LA} \approx 0.9$ at the BZ boundary was obtained by fitting pressure-Raman data to the temperature-dependent thermal expansion [8.27].

The mode γ's for BZ boundary TA phonons in most tetrahedral semiconductors are anomalous in that they are negative. This means that the effective force constants for these modes weaken with pressure, i.e., the corresponding springs become softer rather than stiffer. Some modes in molecular solids have $\gamma_i < 0$ because a *macroscopic* compression actually causes a slight expansion in a particular direction, as for intrachain optical vibrations in trigonal Se [8.57]. This is not the case here; the mode softening corresponds to a real weakening of the effective repulsive forces determining short wavelength shear acoustic vibrations. $\gamma_{TA(X)}$ is -1.4 for Si, -0.72 for GaP, -1.2 for ZnS, and $\gamma_{TA(L)}$ exhibits similar large negative values (Table 8.1). In fact, the available data for these materials show that for the lowest energy acoustic branch negative γ_i of this magnitude apply to a rather large set of modes covering most of the BZ boundary and extending $\sim 1/3$ into the zone (Figs. 8.15–17). Tables 8.1, 2 show that a similar situation pertains to other tetrahedral semiconductors, with the notable exceptions of diamond [$\gamma_{TA(X)} \approx 0.4$] [8.39] and CuI [$\gamma_{TA(L)} \approx 3.0$] [8.58, 59]. The reason for this is not presently understood.

Along low-symmetry directions, where the shear branches are not doubly degenerate, data are more sparse. For the second (intermediate energy) acoustic branch near the K-point, viz. $\boldsymbol{q} = (\pi/a\sqrt{2})(110)$, $\gamma_i = -0.3$ for Si and ZnS and $\gamma_i = 0.15$ for GaP. Thus we expect small negative or positive mode γ's for this branch near the BZ boundary.

Also listed for completeness in Table 8.1 are the γ_i for $\boldsymbol{q} \approx 0$ acoustic modes (from Brillouin scattering or pulse-echo measurements) computed by replacing

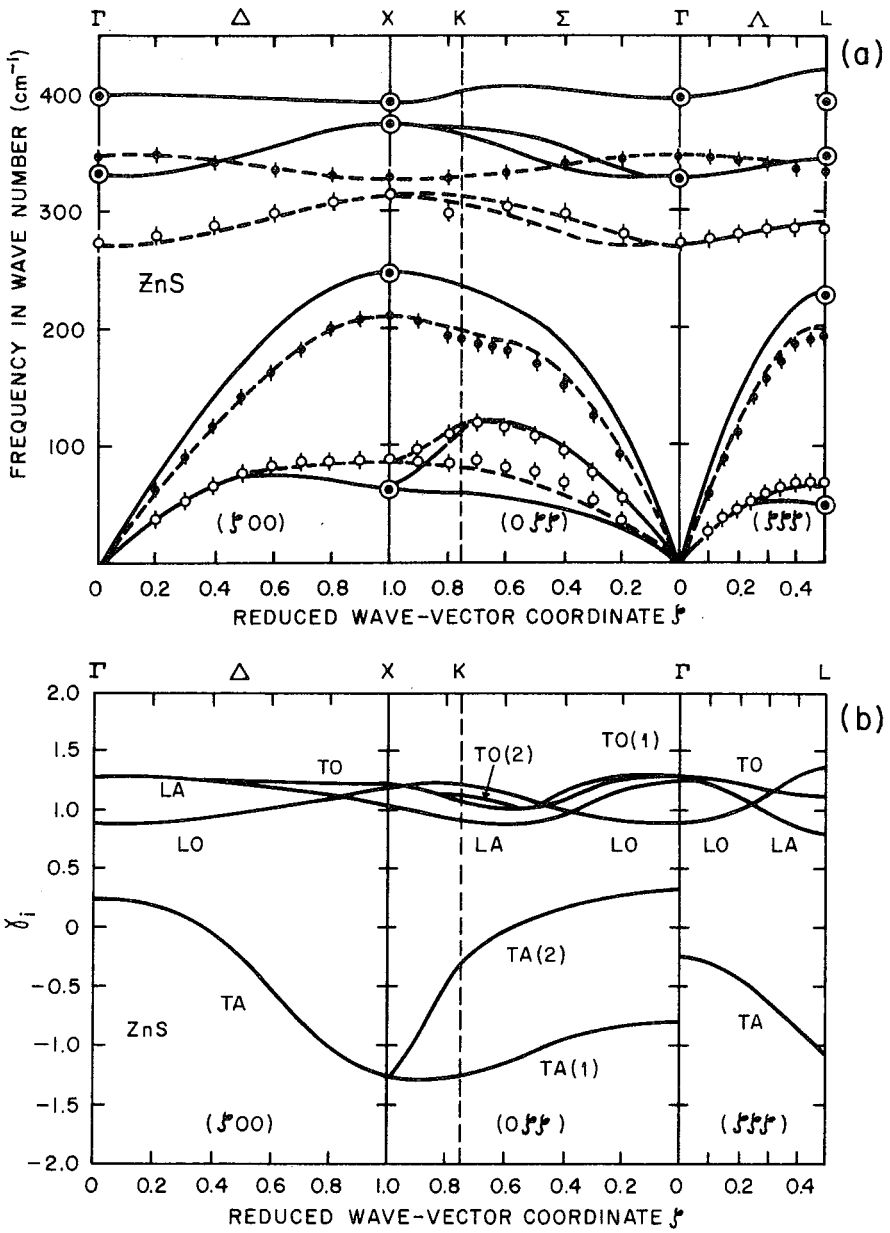

Fig. 8.18. (**a**) Calculated phonon dispersion (300 K) of ZnS at $P=0$ (*dashed curves*) and $P=150$ kbar using an 11 parameter rigid-ion model. $P=0$ dispersion fit to neutron scattering data (*solid* and *open points*); $P=150$ kbar dispersion fit to pressure-Raman data (*circled points*). Note close agreement with Fig. 8.17. (**b**) Corresponding mode Grüneisen parameter dispersion relations for ZnS. After [8.56]

B in (8.11) by the longitudinal and two shear elastic moduli c_{11}, c_{44} and $(c_{11}-c_{12})/2$, respectively. Only for the latter mode [corresponding to distortion parallel to $(1\bar{1}0)$, $\boldsymbol{q}$ parallel to (110)] is γ_i negative in some cases. However, the reported values $0.2 \geq \gamma_i \geq -0.5$ are generally small compared to the corresponding BZ boundary TA(K or X) mode parameters [8.60].

The above trends are summarized in the frequency dispersion curves of Figs. 8.15–17 where arrows (for Si and GaP) and dashed curves (for ZnS) indicate the response to pressure based solely on the Raman observations near critical points. For ZnS (Fig. 8.17), the dashed curves are a semiquantitative estimate of the frequency dispersion at 150 kbar (the transition pressure to an opaque phase). Similar estimates have been made for ZnSe and ZnTe [8.54, 61]. These totally empirical estimates compare favorably [see Fig. 8.18a for ZnS] with the more rigorous results of an 11 parameter semiempirical rigid-ion model for the zinc chalcogenides that will be discussed below [8.56]. Figure 8.18b shows the mode Grüneisen parameter dispersion curves for ZnS obtained from this calculation. From the data in Tables 8.1, 2, it would be straightforward to sketch similar high-pressure frequency dispersion curves and Grüneisen parameter dispersion curves which exhibit the correct behavior for other materials.

8.3.3 Thermal Expansion

Most tetrahedral semiconductors (except diamond and CuI) have a negative low temperature thermal expansion α [8.62]. [Of course, for $T \to 0$, $\alpha(T) \to 0$]. *Blackman* [8.16] suggested on the basis of (8.10) that this anomalous behavior stemmed from negative γ_i for low frequency BZ boundary TA modes.

Pressure-Raman measurements have made it possible to explicitly demonstrate Blackman's conjecture for several of the materials in Tables 8.1, 2. For Si, *Weinstein* and *Piermarini* [8.27] exploited the aforementioned similarity between the two-phonon Raman spectrum and the density of states to perform the summation over modes in (8.10). Interpolating γ_i linearly with frequency between critical points, they obtained the $\alpha(T)$ curves shown in Fig. 8.19. By fitting to $\alpha(300\ \mathrm{K})$, $\gamma_{\mathrm{LA,LO}} \approx 0.9$ was deduced for the (unmeasured) BZ boundary longitudinal modes. A scheme for weighted averaging over high-symmetry directions was employed by *Soma* [8.22] in similar calculations. Also *Talwar* et al. [8.56] performed a more detailed calculation for ZnS, ZnSe, and ZnTe (Fig. 8.20) using the density of states and mode γ's derived from their rigid-ion model.

The mode γ's are microscopic quantities depending on interatomic forces; the thermal expansion [or by (8.10), γ_{av}] is an independently measurable macroscopic quantity. Thus, the agreement with experiment in Figs. 8.19, 20 is excellent corroboration of the pressure-Raman results. However, the macroscopic anomaly of negative thermal expansion has merely been traded for the microscopic anomaly of pressure-induced softening of BZ boundary TA phonons, which is not well understood at present. We shall comment further on this in relation to lattice dynamics theory.

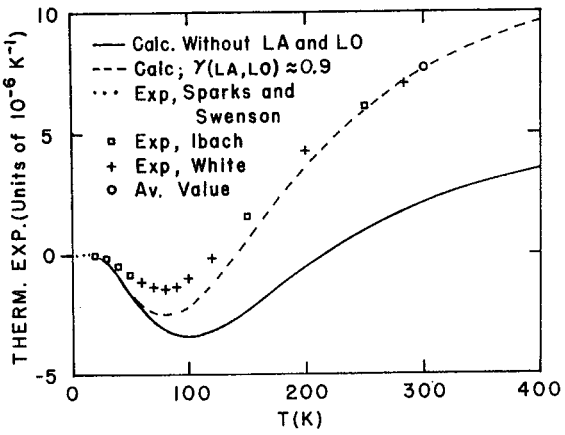

Fig. 8.19. Volume thermal expansion $\alpha(T)$ of Si calculated using pressure-Raman data compared with experiment (see text). After [8.27] and references therein

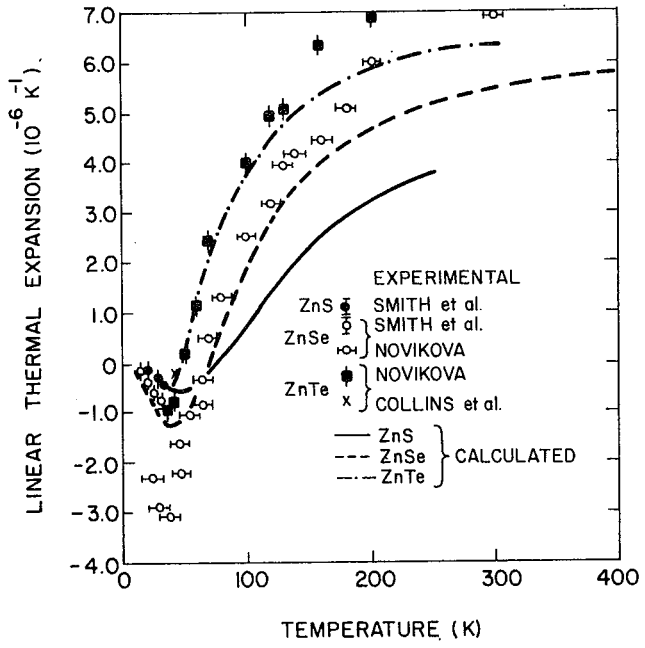

Fig. 8.20. Linear thermal expansion of ZnS, ZnSe, ZnTe calculated using the 11 parameter rigid-ion model of *Talwar* et al. compared with experiment. After [8.56] and references therein

8.3.4 Implications for Lattice Dynamics Theory

The pressure-Raman results just described provide important input, and also stringently test various lattice dynamics models. These divide into two broad classes: those employing semiempirical force constants such as the rigid-ion [8.56, 63] or shell [8.64] models and the microscopic theories based on the dielectric matrix formalism [8.65–67] or the total energy density functional [8.68, 69] approach. We shall discuss these classes in order.

Dolling and *Cowley* [8.64] and *Jex* [8.70] introduced anharmonic terms of third and/or fourth order (in the harmonic displacements) into shell model expansions of the interatomic potential. In [8.64], third-order 2-body forces between nearest neighbors were included, leading to two parameters, which were fit to the temperature-dependent thermal expansion. Mode γ's were calculated for $\boldsymbol{q}$ along the (001) and (111) directions for Ge. Considerable dispersion was found with negative but underestimated γ_{TA} at the BZ boundary. Calculated γ values ranged between 1.6 and -0.4 which is the correct magnitude (Tables 8.1, 2). *Jex* [8.70] followed a similar procedure, except that third-order terms to second neighbor, and for Ge, fourth-order terms to first neighbor were included. The model parameters were determined for C, Si, and Ge by fitting to $\gamma_{av}(T)$. Similar results were obtained ($-0.6 \leq \gamma_i \leq 1.4$) with $\gamma_{TA} < 0$, but γ_{TA} was again underestimated at the BZ boundary. *Bienenstock* [8.71] simulated a shell model for Ge by dividing a given phonon frequency into first neighbor rigid-ion and dipole-dipole contributions. The former were determined by the elastic constants for which the pressure dependence was taken from experiment. The latter were assumed to scale as $1/V^n$, leading to the single parameter n which was fit to $\gamma_{av}(T)$. Again, considerable dispersion was found for the mode γ's throughout the BZ ($-0.4 \leq \gamma_i \leq 1.8$), with $\gamma_{TA} < 0$ but too small at the BZ boundary.

These anharmonic potential parametrization models give the correct magnitude for the mode γ's. However, to reproduce accurately the measured dispersion of γ_i, higher order and more distant forces would have to be included. The proliferation of parameters would then have little physical meaning, so that a different approach is desirable. If an accurate harmonic model with a limited number of semiempirical parameters is known for $P=0$, such an option is available. One simply measures the pressure dependence of enough phonon frequencies to determine all the parameters, and then recalculates the entire phonon dispersion at each pressure. This fact was first applied by *Vetelino* et al. [8.63] to ZnTe using a 4 parameter rigid-ion model. The three elastic constants, $\omega_{TO(\Gamma)}$ and $\omega_{LO(\Gamma)}$ (all measured as a function of pressure) were used as input data. They found $-0.2 \leq \gamma_i \leq 1.8$ which is in reasonable agreement with experiment (Table 8.1), but again the negative γ_{TA} were too small. *Talwar* et al. [8.56] used an 11 parameter rigid-ion model in a similar calculation for ZnS, ZnSe, and ZnTe. The pressure-dependent input data were the elastic and lattice constants, and the Raman frequencies at Γ, X,L, and K. The predicted frequency and mode γ dispersion curves, shown in Fig. 8.18 for ZnS, are in excellent agreement with experiment [8.54], even for the BZ boundary TA modes. The computed Debye temperature, γ_{av}, and thermal expansion (Fig. 8.20) also agree with experiment at low T but deviate somewhat at high T. For all three materials the calculated BZ boundary TA branches do not retain their flatness at high pressure. This may be an artifact of the calculation, since at $P=0$ the flatness is maintained as the BZ boundary TA frequencies decrease through the series ZnS, ZnSe, ZnTe. The flatness for $P>0$ probably requires the inclusion of bond-charge effects, which are not treated in a rigid-ion model.

The bond-charge picture [8.72] is a convenient vehicle for including near range strictly covalent forces – viz., those arising from off-diagonal screening in

the dielectric matrix formalism [8.65] (see below). Born-von Karman models may require forces to fifth neighbor to achieve equivalent accuracy [8.73]. For covalent semiconductors at $P=0$, *Weber's* [8.74] dynamic bond-charge model succesfully represents the BZ boundary TA phonons. Their low frequency and flat dispersion results because the effective ion bond-charge force is small compared to the force between bond charges. Consequently,for TA(X) and nearby modes, the ions vibrate like Einstein oscillators [at $\sim\omega_{\mathrm{TA}(X)}$] within a nearly rigid lattice of *bond charges*. At least for C, Si, and Ge, there is no reason why the 4(or 5) parameter models of [8.74], in combination with available Raman and elastic constant pressure data, could not be employed to calculate high-pressure dispersion curves. However, this has not yet been done.

The pressure-Raman results severely test various microscopic lattice dynamics theories because they require these models to reproduce not only the $P=0$ dispersion curves but also the proper trends as the lattice constant is varied. Two microscopic pseudopotential-based approaches, the dielectric matrix (DMP) [8.65] and the density functional (DFP) [8.75] formalisms (P stands for pseudopotential in these abbreviations) have met with reasonable success in calculating pressure-dependent phonon properties for semiconductors.

Turner and *Inkson* [8.66] calculated the phonon dispersion at elevated pressure for C, Si, and Ge using the DMP formalism with a Shaw-type pseudopotential [8.76]. The reciprocal lattice Fourier components of the dielectric function $\varepsilon_{GG'}$ were computed in the Wannier representation. However, to simplify the inversion of $\varepsilon_{GG'}$, the extreme tight-binding approximation was used away from the BZ center, but with off-diagonal elements scaled to agree with a more exact $\boldsymbol{q}=0$ treatment. Using the measured pressure dependence of the electronic band structure and the lattice constant, these authors obtained good agreement with experiment for $\omega_{\mathrm{TA}(X)}$, with the pressure-induced softening well reproduced (Fig. 8.21). They confirm that off-diagonal screening must be included to describe properly the bond-charge (noncentral) forces crucial to the BZ boundary TA modes. *Porod* et al. [8.67] also employed the DMP formalism, but in a plane-wave representation, to calculate the pressure dependence of $\omega_{\mathrm{TO}(\Gamma)}$ and $\omega_{\mathrm{LO}(\Gamma)}$. They simplified the inversion of $\varepsilon_{GG'}$ and simultaneously

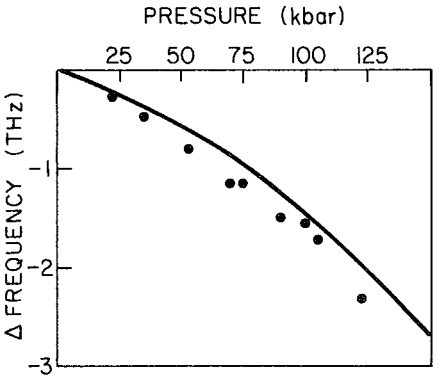

Fig. 8.21. DMP calculation of pressure induced softening of the TA(X) frequency in Si (*solid curve*) compared with experiment (*points* [8.27]). After [8.66]

satisfied charge neutrality by excluding all off-diagonal elements except ε_{OG} and ε_{GO}. These elements were found to be unimportant for TO(Γ) but very important for LO(Γ) and thus e^* (the specific calculation for the pressure dependence of e^* by this method was discussed earlier in Sect. 8.3.1). Reasonable mode γ values were obtained for the tetrahedral semiconductors, e.g., $\gamma_{\mathrm{TO}(\Gamma)}=1.1$ for GaAs compared to 1.4 from experiment [8.42].

The second microscopic approach to predicting pressure-dependent phonon properties in tetrahedral semiconductors employs the DFP formalism to calculate the total energy as a sum of kinetic, electron-ion, electron-electron, ion-ion and exchange-correlation terms [8.75]. At each volume the total energy is computed for the equilibrium atomic configuration, and for the configuration distorted by a given phonon eigenvector (frozen phonon). The harmonic expansion of this energy difference gives the phonon frequency at that volume.

Wendel and *Martin* [8.77] calculated TO(Γ), TA(Γ) (corresponding to $c_{11}-c_{12}$) and TA(X) for Si by this method. A local pseudopotential carried to partial self-consistency was used. The γ_i show the correct trends with $\gamma_{\mathrm{TA}(X)}<0$; this calculation links the softening of TA(X) to the increasing dominance with pressure of ion-ion forces over the electron-electron contribution. In fact, electron-electron interactions (i.e., forces between bond charges) are found to be essential for stabilizing the lattice against the TA(X) distortion.

Yin and *Cohen* [8.68] employed the DFP formalism to predict several static and dynamic properties of group IV materials. For a given structure the only input to their totally self-consistent nonlocal pseudopotential scheme was the atomic number. They also computed γ_i for Si at the Γ and X points. The predicted and measured γ_i agree *within* the limits of experimental accuracy (Table 8.1). In particular, the success for $\gamma_{\mathrm{TA}(X)}$ shows that covalent forces acting via the bond charges and arising from off-diagonal dielectric screening are properly included.

A self-consistent DFP calculation using local pseudopotentials was very recently reported by *Kunc* and *Martin* [8.50] for GaAs. The results also agree well with experiment except for the calculated $\gamma_{\mathrm{TA}(X)}=-3.48$, which is negative but too large (Table 8.1). These authors found that anharmonic contributions are very important for TA(X) in GaAs.

8.4 Changes in Phonon Line Shape with Pressure

8.4.1 Phonon-Phonon Interactions

So far our discussion of mode γ's has assumed the quasi-harmonic approximation. This applies when anharmonic terms are small perturbations to the atomic potential. Then $\Gamma_i/2 \ll \omega_i$ in (8.4), and there will be a well-defined Raman peak at the quasi-harmonic frequency ω_i. However, ω_i differs slightly from its harmonic value (appropriate for $T=0$ and $P=0$) by the real part of the phonon self-energy due to anharmonic interactions; it is this term which causes ω_i to shift

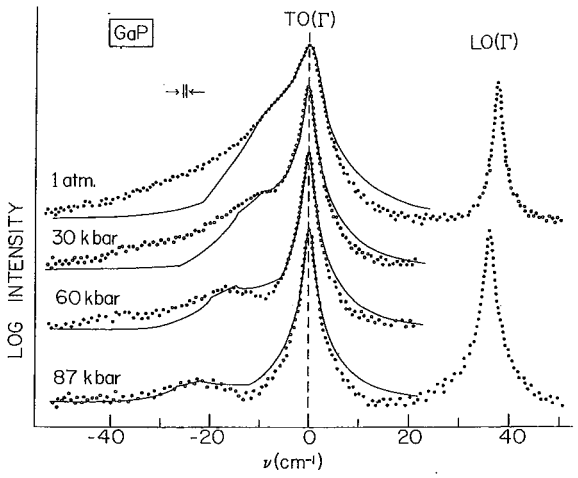

Fig. 8.22. Semilog plot of measured TO(Γ) and LO(Γ) Raman spectra (300 K) of GaP at various pressures (*points*). Calculated TO(Γ) line shape using (8.4, 16) (*solid curves*). Spectra were shifted horizontally to coincide at TO(Γ) and displaced vertically. After [8.78]

with pressure. The imaginary part of the self-energy gives the peak half width $\Gamma_i/2$. We now consider cases where $\Gamma_i/2$ also shows pronounced pressure dependence.

One of the clearest examples is the TO(Γ) Raman peak of GaP, shown as a function of pressure in Fig. 8.22 after [8.78]. At $P=0$ this peak is asymmetrically broadened toward lower energy, whereas LO(Γ) is sharp and symmetric. Under pressure the TO(Γ) peak becomes symmetric, and a weak sideband appears about 23 cm^{-1} below $\omega_{TO(\Gamma)}$. The width of LO(Γ) is relatively unaffected by pressure. *Barker* [8.79] conjectured that the $P=0$ broadening was due to the anharmonic decay of TO(Γ) into a nearly degenerate continuum of TA+LA combinations near the X-point, TA+LA($\sim X$). He described this by a frequency-dependent Γ_i in (8.4). *Weinstein* [8.78] proposed that the different pressure shifts of TO(Γ) and TA+LA($\sim X$) would decrease this resonant interaction, thereby altering $\Gamma_i/2$ for TO(Γ) sufficiently to explain the induced line shape changes.

The theory of anharmonic phonon decay has been discussed by several authors [8.80, 81]. The contribution of the decay TO(Γ)$\rightarrow$TA+LA($\sim X$) to $\Gamma_i/2$, a width parameter that is now expected to be frequency dependent, can be calculated in perturbation theory. The result is [8.78]

$$\frac{\Gamma_i(\omega)}{2} = 18\pi(n_{TA}+n_{LA}+1)|W_{av}|^2 \varrho_2(\omega). \tag{8.16}$$

Here W_{av} is the effective third-order interaction strength, and the main frequency dependence arises from the two-phonon density of states $\varrho_2(\omega)$ due to

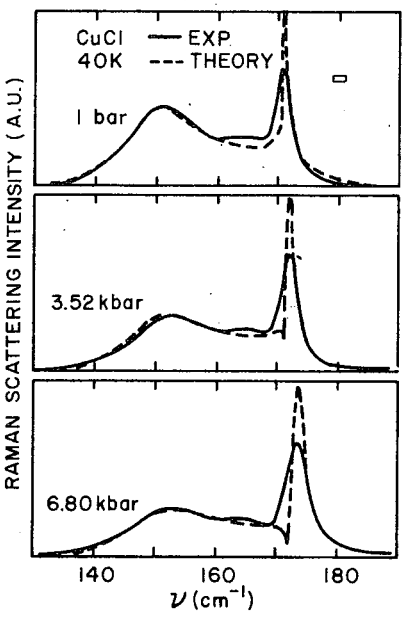

Fig. 8.23. Measured (*solid curve*) and calculated (*dashed curve*) Raman spectra in region of the TO phonon of CuCl as a function of pressure. Box to the right defines uncertainty. After [8.83]

TA+LA($\sim X$) combinations. The thermal factor in parenthesis comes from considering the competition between the decay TO(Γ)→TA+LA($\sim X$) and the reverse process. Using (8.16) and computing $\varrho_2(\omega)$ from the measured dispersion curves at $P=0$ [8.82], the solid line fits shown in Fig. 8.22 were obtained [8.78]. W_{av} was found to be $\sim 2\%$ of $\omega_{TO(\Gamma)}$ at $P=0$, and W_{av} decreased by $\sim 0.4\%$/kbar. A shift of $+0.2\ \mathrm{cm}^{-1}$/kbar was deduced for TA+LA($\sim X$), from which $\gamma_{LA(X)} \approx 1.0$ was obtained [using the $\gamma_{TA(X)}$ value from Table 8.1]. Since TO(Γ) shifts by $0.45\ \mathrm{cm}^{-1}$/kbar, the near degeneracy responsible for the asymmetric broadening is broken at high pressure as expected. Note also [see (8.2−4, 16)], if $|\omega_{TO(\Gamma)} - \omega| > \Gamma_i/2$, then $d^2\sigma/d\Omega\, d\omega_s \propto \varrho_2(\omega)$, which explains the density of states-like sideband that persists at high pressure.

Shand et al. [8.83] applied a similar treatment to the pressure dependence of the anomalous TO(Γ) Raman line shape in CuCl. This is shown in Fig. 8.23. The anharmonicity is much larger for CuCl than for GaP, causing a greater distortion of the TO(Γ) peak. These authors calculated both the real and imaginary parts of the self-energy due to the interaction of TO(Γ) with an assumed two-phonon continuum having a M_3-type square root singularity. Their 7 parameter fits (see dashed curve in Fig. 8.23) reproduce the 40K line shape quite well at each pressure, and account for the induced decrease in the relative strength of the broad low-energy band compared to the sharp high-energy peak.

Despite the apparent success of this analysis, *Vardeny* and *Brafman* [8.84a] have maintained that CuCl is so anharmonic that a perturbation treatment is inappropriate. They proposed a disorder model in which the anharmonic potential for the Cu^+ ion has two types of minima. CuCl would then

be an "alloy" with Cu^+ ions occupying both sites, giving two distinct systems of optical modes. This would account for the dual-peaked TO(Γ) Raman spectrum at $P=0$. It was argued that under pressure, increased repulsive forces would skew the population of sites against the broad low-energy peak, thereby explaining the observed intensity changes (Fig. 8.23).

In the past, pressure-Raman studies of frequency shifts have often taken precedence over measurements of (usually more subtle) line-shape changes. These examples illustrate that more work in this area could be quite fruitful. (For example, see the very recent work by *Schmeltzer* and *Beserman* [8.84b] invoking fourth order anharmonic coupling between 2TA(X) and TO-TA(X) to explain pressure-induced changes in the two-phonon Raman line shape and intensity of ZnSe).

8.5 Phase Changes

Under compression all solids eventually exhibit one or more phase transformations. These span the range from drastic changes of volume, symmetry and electronic properties to subtle shifts of lattice parameters. Raman scattering can help identify the symmetry of a high-pressure phase through the assignment of new structure. It can also investigate behavior antecedent to a transition by studying modes which soften under pressure. Here we discuss Raman investigations of pressure transformations in the tetrahedral semiconductors. We focus on two illustrative cases: the zincblende→rhombohedral→tetragonal changes of CuI, which offer an excellent example of structural identification, and the metallization transition in groups IV, III–V and II–VI materials, which demonstrates possible antecedent behavior.

Unfortunately, space does not permit us to discuss pressure-Raman studies of transitions in many ionic, ferroelectric and ferroelastic solids; the interested reader is referred to several excellent recent reviews [8.11–15].

8.5.1 Transitions in CuI

Often the pressure transitions in tetrahedral materials occur via atomic displacements along one of the initial high-symmetry directions. The resulting reduced-symmetry structures exhibit changes in the Raman selection rules determining the number of active modes. For example, one way (among others) to achieve the zincblende (zb)→NaCl structural change (known for many group II–VI materials [8.85, 86]) is to increase the cation-anion sublattice displacement along (111) to 1/2 of a cubic body diagonal. Whereas the zb phase had two Raman-active lines, the new NaCl phase has none, owing to the presence of inversion symmetry.

The structural sequence zincblende ($P=0$)→rhombohedral (14 kbar)→tetragonal (41 kbar) of CuI illustrates a case for which the Raman spectra change but do not disappear. Figure 8.24 shows the spectra corresponding to these structures and the pressure shifts of the observed peaks after *Brafman* et al.

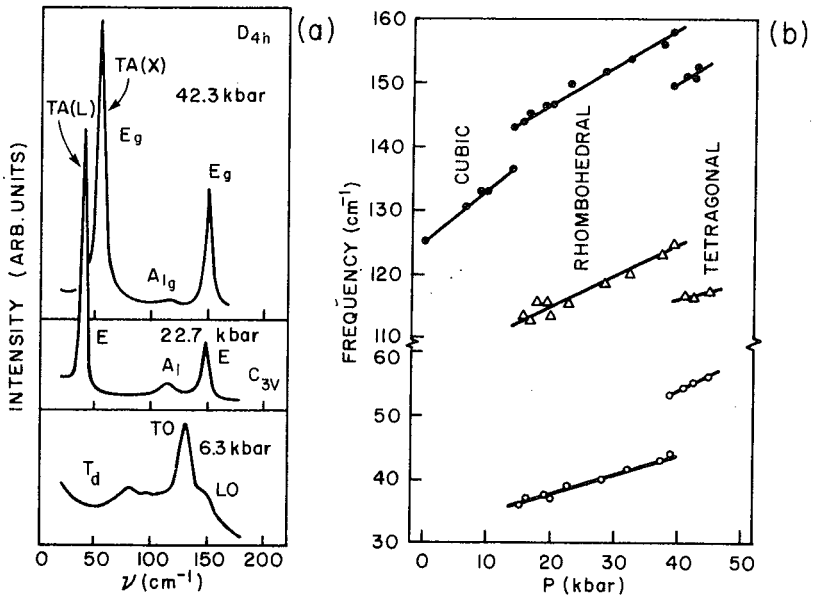

Fig. 8.24. (**a**) Raman spectra (300 K) of CuI in the zincblende (T_d), rhombohedral (C_{3v}) and tetragonal (D_{4h}) phases. TA(L) and TA(X) designate phonon origins in the zincblende BZ. (**b**) Frequencies of observed peaks versus pressure. After [8.58]

[8.58]. In that work, LO phonons could not be followed as a function of pressure because LO scattering was either hidden in the indicated shoulder for zb, or it was simply unobserved for the other phases.

The rhombohedral (trigonal) phase can be achieved by a deformation along the cubic (111) axis in which alternate planes of Cu atoms and alternate planes of I atoms are displaced. The new unit cell is a rhombohedron exactly twice the volume (scaled by the changed lattice parameter) of the original primitive rhombohedron of the fcc lattice. In particular the repeat distance along (111) is doubled. This transformation is depicted in Fig. 8.25a.

The doupling along (111) in real space implies a halving of the BZ along the corresponding (111) direction in reciprocal space such that the cubic L-point is brought to $\boldsymbol{q}=0$. We then expect four new $\boldsymbol{q}=0$ frequencies corresponding to TA(L), LA(L), TO(L) and LO(L) in the zb phase. Since there are now four atoms per unit cell, the trigonal symmetry (C_{3v}) mandates $3E+3A_1$ optic modes that are both Raman and ir active. The original cubic TO(Γ) and LO(Γ) account for $1E$ and $1A_1$, while the folded TA(L), TO(L), and LA(L), LO(L) phonons account for the other $2E$ and $2A_1$ modes, respectively. Given the nonobservation of weak LO scattering and the near degeneracy of TO(Γ) and TO(L) in the zb phase (known from $P=0$ inelastic neutron data [8.87]), three Raman peaks are expected in agreement with experiment (Fig. 8.24a) [8.58].

The relationship between the tetragonal and zb phases of CuI can be seen in Fig. 8.25b. There the primitive tetragonal cell of the high-pressure phase is

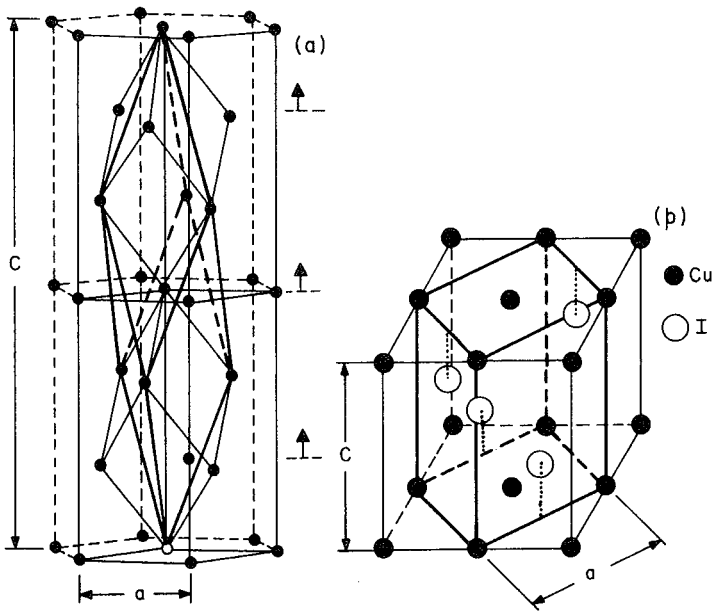

Fig. 8.25. (**a**) Rhombohedral cell for high pressure phase of CuI (*heavy lines*) in a hexagonal supercell (*thin lines*). Original *fcc* rhombohedrons (also *thin lines*) are shown. Arrows indicate displacement of atomic planes during transition. (**b**) Tetragonal cell for CuI (*heavy lines*) inside cubic zincblende cell. After [8.58]

inscribed in the unit cube of zb. The main change is a (001) displacement of the Cu atoms originally at the center of the side faces; in the new structure these atoms lie in the basal plane. The c/a ratio of the tetragonal cell changes little from its cubic value of $\sqrt{2}$. This is quite different from the tetragonal transition in Si and InSb to be discussed below (Sect. 8.5.2). The tetragonal cell also has twice the scaled volume of the primitive fcc rhombohedron. This time the BZ is halved along the (001) c-axis so that the corresponding cubic X-point is folded to $\boldsymbol{q}=0$.

With four atoms per tetragonal cell, the D_{4h} symmetry requires $1A_{1g}$, $1B_{1g}$, $2E_g$ (Raman active) and $1A_{2u}$, $1E_u$ (ir active) optical modes. The cubic LA(X), LO(X), TA(X), and TO(X) phonons transform as A_{1g}, B_{1g}, E_g, and E_g, respectively, while the original TO(Γ) and LO(Γ) modes acquire the ungerade label and become Raman inactive. Given again the nonobservation of LO scattering, three Raman peaks are expected and observed (Fig. 8.24a). They are all derived from phonons at the X-point of the fcc BZ.

In Fig. 8.24b the low-frequency modes corresponding to TA(X) and TA(L) have $\gamma_i > 0$ for the rhombohedral and tetragonal phases of CuI, in exception to most other tetrahedral semiconductors (Tables 8.1, 2). *Brafman* et al. [8.58] concluded that $\gamma_{\mathrm{TA}(L)}$ and $\gamma_{\mathrm{TA}(X)}$ are probably positive in zb CuI also because no negative low temperature thermal expansion is observed. A reason for this may be unusually strong anharmonicity in copper halides [8.83, 84a]. In contrast, $\gamma_{\mathrm{TA}(L)} < 0$ in the zb phases of CdS, ZnO [8.38, 43], ZnS [8.88] and AgI [8.89] was

deduced from the observed negative γ_i of the low frequency E_2 mode in the corresponding wurtzite phases; likewise, $\gamma_{TA(X)} < 0$ is implied by the negative γ_i measured for low frequency Γ_5 phonons in chalcopyrite structure $CuGaS_2$ and $AgGaS_2$ [8.90]. This raises the question as to what extent the γ_i of Raman forbidden BZ boundary phonons can be surmised from the γ_i of corresponding allowed BZ center modes in a lower symmetry phase of the same material. It is not clear that γ_i (or ω_i) can be extrapolated across a jump discontinuity (Fig. 8.24b) at a phase transition when the atomic positions (and therefore the atomic forces) change substantially, as for the zb→tetragonal transition of CuI.

8.5.2 Pressure-Induced Metallization – Possible Antecedent Behavior

The prototypical transformation of this class is the gray tin [semiconducting, diamond structure (fcc)] to white tin [metallic, body-centered tetragonal (bct)] transition, which actually occurs in tin at $P=0$ and $T=286$ K. In finite bandgap semiconductors, similar phase changes occur only at higher pressure [8.86, 91–93]. The transitions are first order with large volume decreases of 10–20 %. *Klement* and *Jayaraman* [8.85] have reviewed the complicated phase diagrams and structures that apply. For Si, Ge, and Sn (for diamond it is unknown), the final phase has the bct structure; it is metallic, due most likely to overlap of the X-point conduction band minimum (now folded back to Γ) with the valence band [8.94a, b, c]. For those III–V and II–VI materials that have been studied, the bct, NaCl, and several orthorhombic structures have all been reported at high pressure [8.85, 86]. Several of the more ionic compounds – those with Phillips' ionicity >0.3 – remain semiconducting (even if visibly opaque) after the lowest pressure phase change [8.95]; however, the transition still results in a reduced bandgap, signaling a pressure-induced approach toward the metallic state [8.94b, c].

The central question here is to what extent does the softening of BZ boundary TA phonons under pressure constitute antecedent behavior to this metallization transition? The pressure-Raman studies that bear on this issue are those of *Weinstein* and *Piermarini* [8.27] on Si and GaP, *Weinstein* [8.54, 61] on ZnS, ZnSe and ZnTe, *Trommer* et al. [8.42] on InP and GaAs, *Carlone* et al. [8.90] on $CuGaS_2$ and $AgGaS_2$, and *Olego* and *Cardona* [8.96] on Ge.

In [8.27] the phonon dispersion curves of Si and gray-Sn were compared at their respective transition pressures, $P_T \approx 125$ kbar and $P_T = 0$. To do this the ω_i were scaled by the ion-plasma frequency appropriate for each material. The scaling insures that any remaining differences are mainly due to the valence electrons. It was found that at P_T the flat TA branch near the BZ boundary was rather similar in both materials, indicating parallel behavior of the valence electrons for these modes. However, a similar comparison of GaP to α-Sn and to InSb showed no analogous result.

An empirical linear relationship between $\gamma_{TA(X)}$ and P_T that does apply to several compound semiconductors as well as to Si and Ge was first proposed by *Weinstein* [8.54]. Figure 8.26 shows this correlation for Si, GaP, ZnS, ZnSe,

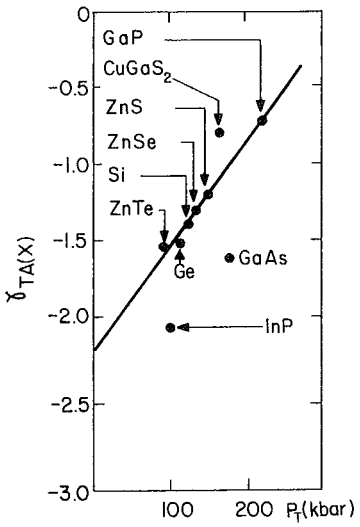

Fig. 8.26. Empirical relationship between the TA(X) mode γ and the metallization transition pressure P_T suggested by *Weinstein* [8.54] (see also [8.42a, 90, 96])

ZnTe [8.54], Ge [8.96], InP, GaAs [8.42, 97] and $CuGaS_2$ [8.90]. (For $CuGaS_2$ the lowest Γ_5-phonon was used; see Sect. 8.5.1). The linearity is remarkable for the first six solids, but an unshown point for $AgGaS_2$ ($\gamma_{\Gamma_5} \approx -4.5$, $P_T = 42$ kbar) falls far afield. Still the trend is clear: the faster the BZ boundary TA frequencies decrease with pressure, the lower is P_T. An alternative empirical correlation for these solids was subsequently suggested by *Carlone* et al. [8.90]. They found that the lowest pressure transition occurred when $\omega_{TA(X)}$ (or its equivalent) had decreased to 0.7 times its $P=0$ value. Although no ω_i actually vanish prior to this first order transition, these correlations demonstrate some antecedent behavior which we now try to relate to the structural and electronic changes that occur.

The fcc→bct structural transition is depicted in Fig. 8.27 for InSb [8.98]. It corresponds to a contraction along the c-axis (001) and an expansion along the normal a-axes such that the bct cell becomes primitive with $c/a < \sqrt{2}$. The (scaled) first BZ is halved, and the X-point is folded back to Γ as for the tetragonal phase of CuI. *Musgrave* [8.99] pointed out that the $\boldsymbol{q}=0$ shear wave governed by $(c_{11}-c_{12})/2$ could drive this distortion. However, *Demarest* et al. [8.100] discounted a simple strain mechanism because large electronic changes (i.e., metallization) are involved. Although the γ_i corresponding to $(c_{11}-c_{12})/2$, from (8.11), are generally small and sometimes negative [8.60], BZ boundary TA phonons have by far the largest negative γ_i (Table 8.1). This indicates that short wavelength TA modes are the primary source of pressure-induced instability in the diamond and zb lattices as suggested by *Phillips* [8.101]. Because the TA branch is flat near X, *i.e.*, $V_{\boldsymbol{q}}\omega_{TA(X)} \approx 0$, the TA($X$) mode sets up an approximate standing wave pattern. Since the group of the X-point in diamond and zb (D_{4h} and D_{2d}) exhibits tetragonal symmetry, this pattern is compatible with a $\boldsymbol{q}=0$ optical phonon in a tetragonal lattice. The observation $\omega_{TA(X)}$ (at P_T) $\approx 0.7\omega_{TA(X)}$ (at $P=0$) shows that the standing wave period undergoes a 30% increase by P_T. Nevertheless, the corresponding distortion

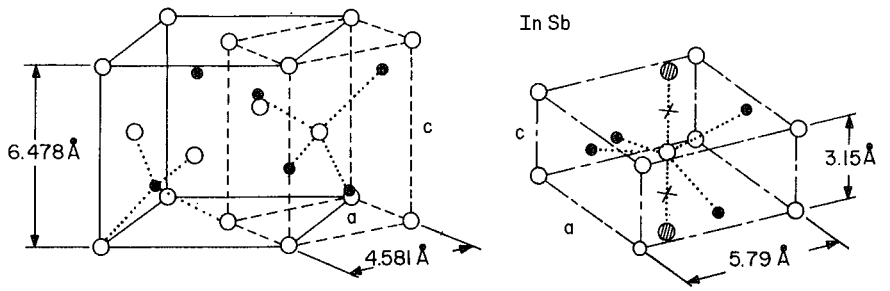

Fig. 8.27. Cubic-to-tetragonal structural change that accompanies the metallization transition in InSb. The nonprimitive bct cell (*dashed lines*) in the fcc lattice becomes primitive after the indicated distortions. After [8.98]

remains dynamic, and the mechanism by which the unstable BZ boundary TA modes are linked to the static structural change is not understood.

The connection between metallization and the softening of BZ boundary TA phonons is likewise unclear. Some insight is provided by the bond-charge model. In *Weber*'s [8.74] treatment, the TA(X) mode corresponds to the ions vibrating within a nearly rigid lattice of *bond charges*. Under pressure, $\omega_{TA(X)}$ decreases because ion bond-charge forces decrease, so that the valence electrons (within the bond charges) become increasingly *decoupled* from the ions in this mode. Within the dielectric matrix formalism [8.65–67] this is caused by a decrease in the relative magnitude of off-diagonal versus diagonal screening. This corresponds to metallization since diagonal screening is strongly predominant in metals.

In principle, the DFP method [8.50, 68, 69, 77] should be able to elucidate any antecedent role for BZ boundary TA modes in the metallization transition. Nevertheless, a clear picture has not emerged. *Wendel* and *Martin* [8.77] showed for Si that $\gamma_{TA(X)} < 0$ resulted from the decreasing importance with pressure of electron-ion and electron-electron energies relative to ion-ion terms. *Maschke* and *Andreoni* [8.69] found that the decrease of the electron-ion interaction caused the transition in ZnSe – this time to a semiconducting NaCl structure. *Yin* and *Cohen* [8.68] demonstrated that the high-pressure structures of Si and Ge should be bct and closely predicted P_T; they also calculated reasonable negative values for $\gamma_{TA(X)}$ (Sect. 8.3.4). However, in each treatment the relationship between the decrease of BZ boundary TA frequencies in the initial phase and the structure, electronic character and onset P_T of the final phase was not explored. Some progress was made in a recent calculation for GaAs by *Kunc* and *Martin* [8.50]. They showed that the total energy as a function of the TA(X) eigenvector amplitude acquired a new minimum at elevated pressure, but they did not examine the uniqueness of this minimum. Also the most recent work of *Cohen* et al. [8.94a, 8.94b] has produced some qualitative insights in terms of pressure-induced changes in the competition between the covalent-bond energy that favors the semiconducting phase, and the Ewald energy (core-core Coulomb interaction) that favors the metallic phase. However, more work along these latest directions is needed to understand the relation to TA(X) mode softening.

8.6 Pressure-Tuned Resonant Raman Scattering

Usually resonant Raman scattering is observed by tuning the incident laser frequency ω_l through various bandgaps which act as poles for the Raman cross section according to (8.2, 5). Alternatively, the bandgap can be tuned through ω_l (or ω_s) by some perturbation. Pressure tuning is an attractive technique for semiconductors in frequency regions not spanned by conventional lasers because the bandgap pressure coefficients are often large – typically ~ 10 meV/kbar. A pressure of 100 kbar can tune a gap through 1.0 eV (~ 2000 Å in the visible). Balancing this advantage is the difficulty of controlling factors that determine the observed intensity during a pressure change (e.g., window and medium depolarization and refractive index, sample orientation, etc.).

There have been very few resonant Raman experiments employing hydrostatic pressure. Our goal here is to illustrate the power of this technique in the hope that it will be more frequently applied. We shall discuss the most studied case, the E_0 gap resonance in GaAs [8.44, 97]. Uniaxial stress has more often been used in resonance measurements, as for the E_1-gaps of Ge, InSb [8.102] and

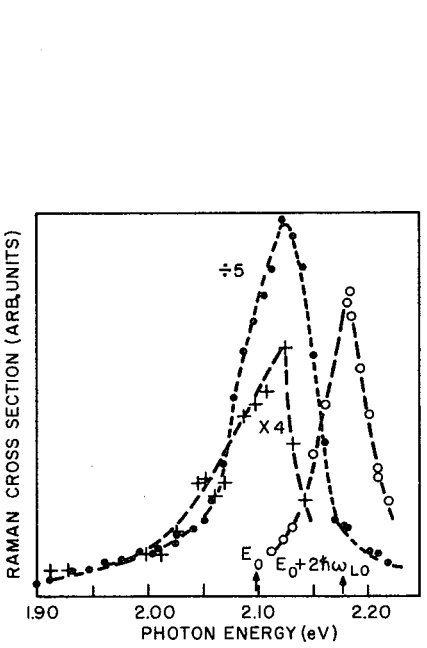

Fig. 8.28

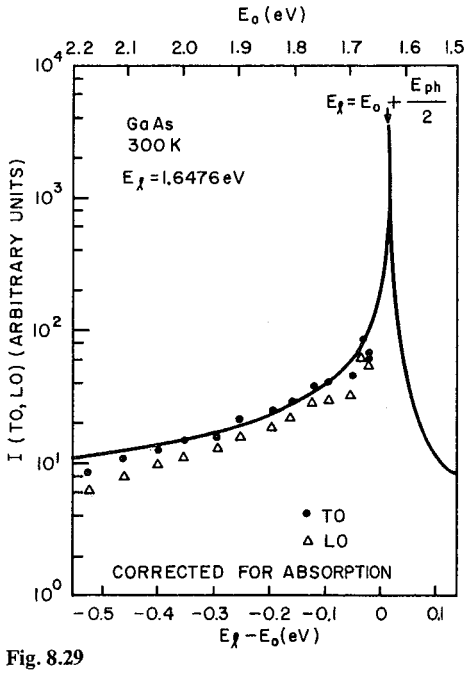

Fig. 8.29

Fig. 8.28. Raman cross section for TO(Γ) (*crosses*), LO(Γ) (*solid circles*) and 2LO(Γ) (*open circles*) in GaAs at 62 kbar (300 K) versus incident laser energy. After [8.97]

Fig. 8.29. Resonance profiles for TO(Γ) and LO(Γ) near E_0 in GaAs. *Solid curve* was calculated using dielectric response theory. After [8.44]

InAs [8.103]. In keeping with the design of our chapter, we do not discuss these, but refer the reader instead to the recent review by *Anastassakis* [8.104].

First we note that in both [8.44, 97], pressure was exploited to make GaAs transparent to the visible laser frequencies used. This increased the Raman signal (over the diamond-cell background) to acceptable limits by virtue of increased sample penetration depth. (The direct E_0 bandgap of GaAs occurs at 1.43 eV at $P=0$, $T=300$ K, and it shifts by $+11.7$ meV/kbar [8.105]). This technique could be used to similar advantage for other opaque semiconductors.

Yu and *Welber* [8.97] combined both pressure and frequency (dye laser) tuning to study the GaAs E_0 resonance. Figure 8.28 shows their resonance profiles at 62 kbar for TO(Γ), LO(Γ) and 2LO(Γ). No attempt was made to analyze the profiles in terms of the dielectric response theory, see (8.2, 5), and the known band structure. Combined tuning allowed these authors to measure the pressure shifts of the profile peaks; these shifts were shown to correspond closely to that of the E_0 bandgap. Thus the shift of an *electronic energy* was found from pressure measurements of *phonon* Raman *intensities*.

Trommer et al. [8.44] did study the resonance profile of TO(Γ) and LO(Γ) in the vicinity of E_0 for GaAs. Their data, obtained by pressure tuning with the laser fixed at $E_l=1.648$ eV, are shown in Fig. 8.29. The fitted solid curve was calculated including 2-band (as in Fig. 8.2), 3-band (similar to Fig. 8.2, but the phonon mixes spin-orbit-split valence band states at $\boldsymbol{q}\approx 0$), and nonresonant contributions to the Raman tensor. This is equivalent to summing terms as in (8.5) over the allowed electronic transitions near the E_0 gap [8.2]. The good agreement indicates that pressure did not substantially alter the electron-phonon coupling strength (i.e., the deformation potential) responsible for one-phonon scattering.

8.7 Molecular Solids

8.7.1 Rationale for Pressure-Raman Studies of Molecular Crystals

Because the forces which bind them are so weak, molecular solids are very soft. Because they are so soft, pressure is ideally suited as an investigate probe for these solids. It is practical to attain very substantial ($>20\,\%$) compressions of the crystal volume and to cause thereby very large ($>50\,\%$) changes in phonon frequencies. Moreover, because it primarily influences the mushy intermolecular volume, *pressure selectively enhances those effects which are specifically associated with the interactions between molecules.*

The simplest conceivable vibrational model of a molecular solid is illustrated in Fig. 8.30. This elementary figure will serve to introduce a few overall aspects of phonon spectra in molecular solids. Later, with the superposition of a simple ansatz to allow for the anharmonicity of the bonds, this simple model will also provide a framework for understanding the overall effect of pressure on the mode frequencies [8.106].

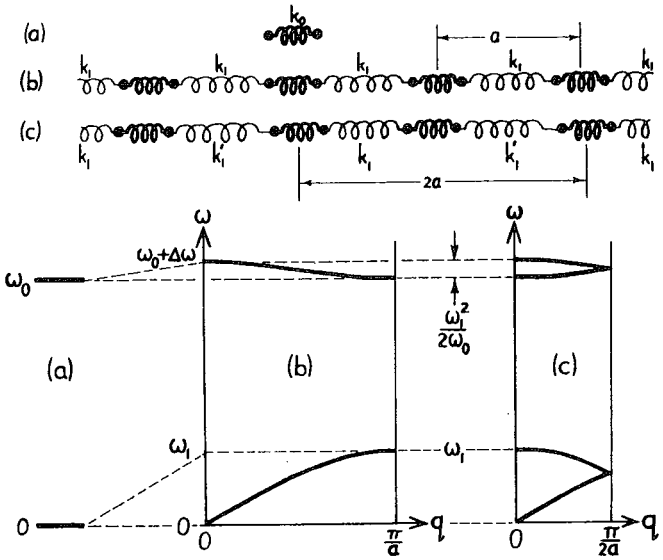

Fig. 8.30a–c. Elementary vibrational models for molecular crystals: (**a**) free molecule, (**b**) linear lattice with one molecule per unit cell, (**c**) dimerized lattice with doubled unit cell. The corresponding phonon dispersion curves are displayed in the lower part of the figure. After [8.106]

Figure 8.30 displays three one-dimensional spring models and their corresponding vibrational spectra (phonon dispersion curves). Figure 8.30a represents a single *isolated* diatomic molecule (in a one-dimensional space) with atoms of mass m held to their equilibrium separation by a spring of force constant k_0. The corresponding vibrational spectrum contains just two frequencies since there are but two degrees of freedom: $\omega = \omega_0$, where $\omega_0 = (2k_0/m)^{1/2}$ is the frequency of the *stretching mode*, and $\omega = 0$, the vanishing frequency of the rigid-molecule *free translation*. Figure 8.30b depicts a simple linear lattice (one molecule per unit cell) of periodicity a in which many such molecules are *weakly coupled* by a set of soft intermolecular springs of force constant k_1 ($k_1 \ll k_0$). For this condensed phase, the simplest model of a molecular solid, the discrete two-line $(0, \omega_0)$ spectrum of the isolated molecule is replaced by a continuous spectrum composed of two narrow and well-separated bands. These correspond to the two phonon branches indicated in (b) in the lower part of Fig. 8.30; $\omega(q)$ in the right half $(0 < q < \pi/a)$ of the one-dimensional Brillouin zone is shown for each branch. The $\omega = 0$ free translation of the isolated molecule gives birth to a low-lying acoustic branch of phonon modes in the crystal, rising up to encompass a low-frequency regime from 0 (at $q = 0$) to ω_1 (at $q = \pi/a$). The ω_0 stretch vibration of the free molecule gives rise to a flat optical-phonon branch spanning the narrow frequency range from ω_0 (at the zone boundary) to $\omega_0 + \Delta\omega$ (at the zone center).

The stretch frequency ω_0 sets the scale for the spectrum of this simple model of a molecular crystal. In the weak-coupling regime $k_1 \ll k_0$, the ratios of the

characteristic frequencies of this elementary model are given by

$$\omega_1/\omega_0 = (k_1/k_0)^{1/2}, \tag{8.17}$$

$$\Delta\omega/\omega_0 = (k_1/k_0)/2. \tag{8.18}$$

These relations reveal the way in which both the flatness ($\Delta\omega \ll \omega_0$) of the optical-phonon branch and the lowliness ($\omega_1 \ll \omega_0$) of the acoustic-phonon branch depend upon the weakness ($k_1 \ll k_0$) of the intermolecular bonding. Consider $\varepsilon \equiv (k_1/k_0)^{1/2}$ as a parameter of smallness in the weak-coupling limit. Equations (8.17, 18) show that ω_1 is of first order in ε while $\Delta\omega$ is of second order.

Real molecular crystals are, of course, far more complex than the oversimplified picture of Fig. 8.30b, but many essential aspects are captured by the model. It is useful to introduce the next stage of complication, shown in Fig. 8.30c, in which the unit cell is doubled in size so as to include two molecules. Introduction of this modest amount of complexity is important because it allows us to make contact with spectroscopy, since the unit-cell doubling places the coupling effects (ω_1, $\Delta\omega$) at the zone center (where they must be in order to be accessible to first-order Raman or far-infrared experiments). In the model of Fig. 8.30c, the pairing-off ("dimerization") is accomplished in the gentlest way by allowing alternate intermolecular force constants to adopt a value k_1' slightly different from k_1.

The situation depicted in Fig. 8.30c, in which a wide disparity exists between the upper set of crystalline frequencies near $\omega \approx \omega_0$ and the lower set of frequencies at $\omega \leq \omega_1$, corresponds to the validity of the *separation approximation* [8.107]. In this approximation, which provides the lowest-order view of a molecular crystal, the intermolecular forces are so weak relative to the intramolecular (covalent) forces that there is a very clear distinction between the high-frequency *internal modes* or *intramolecular modes* (or, simply, *molecular modes*) on the one hand and the low-frequency *external modes* or *intermolecular modes* or *lattice modes* on the other. (The internal-mode/external-mode terminology is the most widely-adopted usage for this dichotomy and will usually be employed here. The lattice-mode usage is misleading, and will be avoided). For external modes, the separation approximation is equivalent to the rigid-molecule approximation. The intermolecular forces are regarded as too weak to appreciably deform the internal structure (covalent bond length, bond angles) within the molecule. Within the context of Fig. 8.30c, k_0 is regarded as infinitely stiff and the molecule may be treated as a single particle of mass $2m$ for the external mode motions described by the two lower ($\omega \leq \omega_1$) branches. The maximum external-mode frequency ω_1 occurs at $q = 0$ when nearest-neighbor intermolecular (k_1, k_1') springs are stretched/compressed in opposite phase to each other. In our simple model, the two bands below ω_1 correspond, for a real molecular crystal, to acoustic phonons and the lowest-lying optical phonons which are constructed of motions similar to the translations and rotations of the free molecule.

A comparison between the $q=0$ phonon spectrum of Fig. 8.30c and the noninteracting-molecule spectrum of Fig. 8.30a thus reveals the main qualitative spectral features which appear when the intermolecular interaction is turned on. In addition to the very low-frequency external modes (ω_1) discussed above, *Davydov-splitting fine structure* ($\Delta\omega$) is imposed on the intramolecular modes (ω_0). Splittings such as this, in which the degeneracy of corresponding excitations on a set of equivalent molecules (equivalent in the context of the crystal-symmetry factor group) is lifted by their mutual interaction, are characteristic of molecular crystals. Variously referred to as *Davydov* or *factor-group* or *correlation-field* splittings, they are simply (as in Fig. 8.30) the classical frequency differences between normal modes of a set of weakly-coupled oscillators. For some situations, it is possible to make a distinction between Davydov splittings and *crystal-field* splittings in which molecular degeneracies of a given molecule are lifted by the low symmetry of the crystalline environment. Such a distinction is a rather artificial one because the same intermolecular interactions provide the root cause of both effects.

One principal rationale for a program of pressure-Raman studies of molecular crystals is provided by the fact that pressure enhances the above-mentioned spectroscopic consequences of intermolecular interactions in the solid state. This effect of pressure is sketched in Fig. 8.31 in a schematic line-spectrum illustration for Raman-active and infrared-active phonons. These vibrational consequences of the condensation into the solid state include the lifting of the free-molecule translations and rotations from zero frequency into the finite-frequency bands of acoustic phonons and (for crystals with several molecules per unit cell – the usual case) low-lying optical phonons, as well as the subtler shifts and splittings of the molecular modes as they develop into the narrow high-frequency optical-phonon branches. With the application of hydrostatic pressure, as indicated in Fig. 8.31, these intermolecular-induced

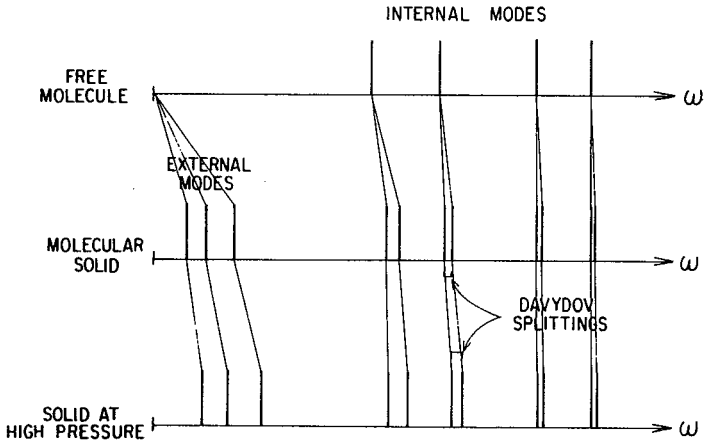

Fig. 8.31. Schematic line-spectrum illustration of the pressure-induced enhancement of intermolecular-interaction effects in a molecular crystal. After [8.108]

effects are enhanced and play a more important role in determining the form of the phonon spectrum.

The value of pressure-Raman experiments for revealing information about intermolecular forces and about the entire hierarchy of interactions which coexist in molecular solids, has been demonstrated in recent studies [8.106, 108–111]. This utility of pressure as a probe of bonding in soft solids provides the main focus of this section of the chapter; it will be discussed in detail in Sect. 8.7.3. An important aspect of this use of pressure-Raman studies is the revelation that the traditional Grüneisen relation which connects phonon frequency with crystal volume breaks down in a dramatic and systematic fashion for molecular solids [8.106, 108] and must be replaced by a more fundamental bond-stiffness/bond-length scaling law.

The search for new solid phases at high pressure is another rationale for pressure-Raman studies on molecular crystals, one which continues the proud tradition pioneered by the vastly extensive volume-versus-pressure measure-

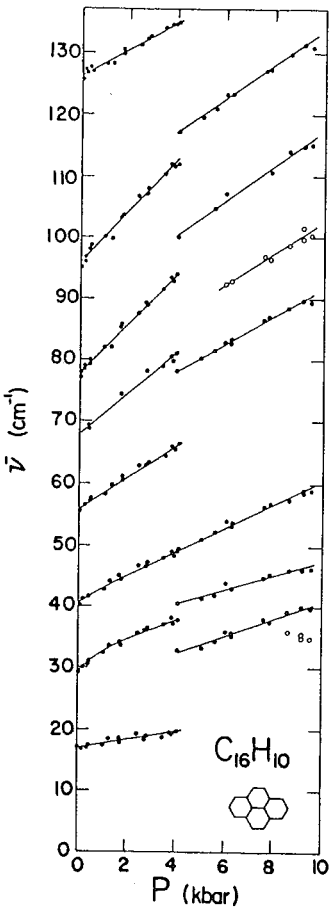

Fig. 8.32. Pressure dependence of Raman-active external-mode frequencies in crystalline pyrene. A first-order transition intervenes at 4.0 kbar. After [8.113]

ments of *Bridgman* [8.112]. Because the forces which are responsible for holding them together are so gentle, molecular solids often undergo solid-solid polymorphic transformations at quite modest pressures. Raman-scattering measurements are very effective in uncovering such phase transitions; an example [8.113] is shown in Fig. 8.32. Pyrene is an organic solid composed of planar ring-system ("aromatic") molecules. The chemical formula and carbon-atom skeleton of the individual molecule is shown at the lower right of the figure; it may be viewed as a graphite fragment bounded by hydrogen on the perimeter. Pyrene is interesting because it is the simplest of a class of organic molecular crystals in which the basic crystallographic building block is a closely-spaced parallel pair (dimer) of planar molecules. The pressure-Raman results shown in Fig. 8.32, along with analogous results obtained with temperature (rather than pressure) as the variable parameter, provided the first direct evidence of a subtle solid-state transition in this material. This figure follows the frequencies, as a function of pressure, of the Raman-active external modes. The discontinuous transformation of the lattice phonon spectrum, observed at 4 kbar, attests to the occurrence of a first-order phase transition. The subtlety of the transition may be appreciated by the fact that dimer pairs survive the phase change, which evidently corresponds to a slight sliding relative displacement of the two molecules within each dimer along with a change in the dimer-dimer conformation. Such a gentle rearrangement of molecules, although nearly indiscernible in the internal-mode high-frequency regime, is easily observed (as shown in Fig. 8.32) when the external-mode frequencies are tracked as a function of pressure.

Pressure-induced molecular-rearrangement solid-solid transitions in molecular crystals, such as the one exhibited by pyrene, are too ubiquitous to cover in this review. (*Bridgman* [8.112] long ago pointed out the high frequency of the occurrence of transformations in this class of solids). Instead, Sect. 8.7.5 will

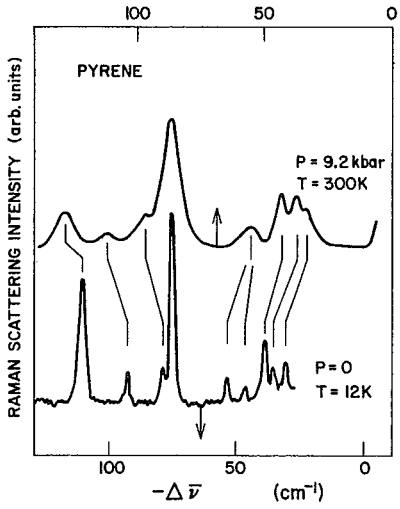

Fig. 8.33. Comparison of the resolution-enhancing aspects of high pressure and low temperature on the external-mode Raman spectrum of pyrene II. After [8.113]

discuss experimental results which bear on the general question of a crossover from molecular to nonmolecular solid-state properties at high pressure.

Before leaving the example provided by pyrene, we show in Fig. 8.33 another illustrative aspect of that study [8.113]. Figure 8.33, which proved the equivalence of the high-pressure form with the form obtained (at $P=0$) at low temperature, displays the correspondence between the high-pressure and low-temperature spectra. At high pressure, the Raman lines are spread over a greater spectral range than at low pressure. Note the low-frequency triplet resolved in both spectra of Fig. 8.33 at around 30 cm^{-1}. At room temperature and low pressure, this triplet is not resolved. High resolution at low temperature is a familiar spectroscopic approach in which the enhanced resolution is achieved primarily via line narrowing at constant splitting. As shown in Fig. 8.33, *high pressure can provide a complementary approach in which enhanced resolution is achieved via increased splitting at constant linewidth.* Other examples of this useful feature of pressure-Raman experiments will appear in the following section. Note that we are dealing throughout this chapter with *isotropic* (hydrostatic) pressure, not with uniaxial stress which is often associated with symmetry-breaking splittings.

A survey of the effect of pressure on the Raman spectra of some simple organic and inorganic molecular solids is presented next in Sect. 8.7.2. The systematics of the response to pressure, and its implications with respect to the extended hierarchy of interaction strengths which coexist in a molecular crystal, are analyzed in Sect. 8.7.3. Here, reference is again made to the simple (but useful) picture of Fig. 8.30 in order to help develop the idea of a bond-stiffness/bond-length scaling law which helps explain the dramatic deviation of molecular solids from the Grüneisen behavior observed for network solids such as the germanium family of semiconductors. In Sect. 8.7.4 we use the pressure-Raman results to dissect the effect of *temperature* into volume-driven ("implicit") and phonon-occupation driven ("explicit") components, and we compare the explicit/implicit mix for modes in molecular crystals with the mix characteristic of covalent and ionic crystals. Section 8.7.5 discusses the search for molecular→nonmolecular transitions at high pressure and touches briefly on a few exotic topics such as the quest for metallic hydrogen and dimensionality (e.g., $2d \rightarrow 3d$) effects.

8.7.2 Pressure-Induced Raman Line Shifts in Simple Organic and Inorganic Molecular Solids

The organic crystal pyrene ($C_{16}H_{10}$), introduced in Figs. 8.32, 33 to illustrate two aspects of pressure effects in molecular solids, is one of a large group of hydrocarbon molecular crystals in which the molecule is built of linked benzene rings. Benzene itself (C_6H_6) is the most basic molecular unit in the aromatic series of organic molecular materials. Figure 8.34 displays the pressure-Raman results of *Ellenson* and *Nicol* [8.114] on crystalline benzene at room temperature.

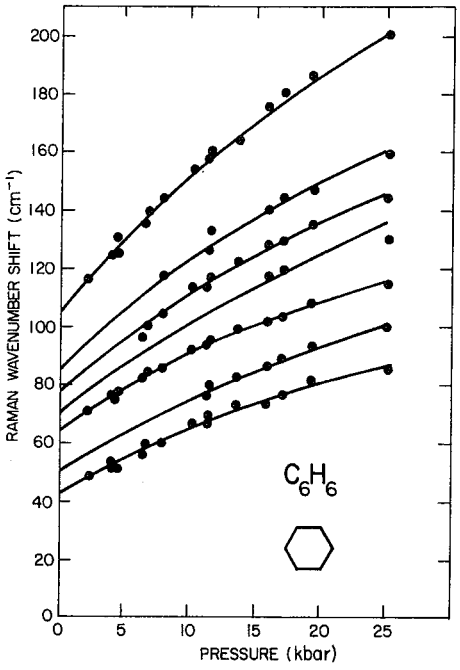

Fig. 8.34. Plot of the wave numbers of the Raman-active lattice bands of benzene I versus pressure. After [8.114]

Shown in Fig. 8.34 are the wave numbers of the observed Raman-active bands of benzene in the external-mode regime, followed up to 25 kbar. Note immediately that this pressure is sufficient to *double* the intermolecular-mode frequencies (i.e., *quadruple* the corresponding force constants). Contrast this enormous effect to that seen in diamond, for which the effect of 25 kbar on the single Raman band is to increase its frequency by a minuscule amount, about one half of one per cent [8.115]. Although this comparison is a bit extreme because, among the hard covalent crystals, diamond is the hardest, it nevertheless conveys a sense of the relatively great sensitivity to pressure of phonons in molecular crystals.

Crystalline benzene has four molecules per unit cell ("unit cell" refers throughout to the primitive unit cell, the smallest translational unit) and each molecule sits on a center of symmetry. The Raman-active modes are therefore the 12 rotational modes (rotational modes are sometimes called librational modes, or *librons*). Note that, in Fig. 8.34, only three lines are resolved at low pressure. As the spectrum spreads out with increasing pressure, more lines are seen via the previously-noted enhanced-resolution aspect of pressure-Raman work. In this study [8.114], a new line was uncovered at high pressure which was never seen earlier (even at low temperature) at $P=0$.

Thus far, organic crystals have been discussed; we now move on to inorganic molecular crystals. A prototypical example is orthorhombic sulfur, an *elemental* molecular crystal composed of eight-atom rings. Unlike the ring molecule in

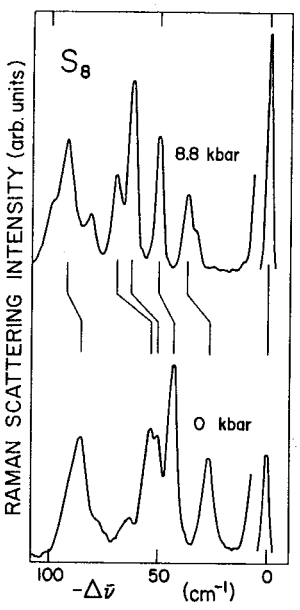

Fig. 8.35. Low-frequency portion of the sulfur Raman spectrum at $P=0$ and at 8.8 kbar. The pressure-induced increases in phonon frequency are indicated for several of the lines. After [8.106]

benzene, the S_8 ring is not planar but is puckered. There are four S_8 rings per unit cell. Figure 8.35 shows the low-frequency region of the Raman spectrum of crystalline sulfur at zero pressure and at a pressure close to 9 kbar [8.106]. Note the two lines near 50 cm^{-1}, barely resolved at $P=0$, are cleanly separated at 9 kbar. Pressure also reveals that the lowest-frequency external-mode band is actually a doublet.

Its extreme chemical simplicity, with only a single type of atom present, has elicited for rhombic sulfur the most thorough *theoretical* treatment of the effect of pressure on the vibrational spectrum of any molecular crystal. *Kurittu* [8.116] has carried out detailed calculations for this crystal, employing a "6–8-exp" atom-atom potential for the van der Waals intermolecular interactions. His analysis included a deformable-molecule model for the S_8 rings. (The latter refinement is necessary for a realistic treatment of sulfur because the rigid-molecule separation approximation is *inadequate* for this crystal: in Fig. 8.35, the modes seen near 85 cm^{-1} have *mixed* internal-mode/external-mode character). The results of these calculations have been compared to the pressure-Raman data of [8.106] and were found to yield satisfactory agreement with experiment.

Lesar et al. [8.117] have succeeded in performing Raman experiments to very high pressure on a very simple molecular crystal, solid nitrogen (N_2). The low-frequency region containing the external modes could not be seen in their experiments, but internal modes (with mode eigenvectors made up of N–N stretching motions of the N_2 molecules) *were* observed and their frequencies are shown in Fig. 8.36. Note the relatively slight influence which pressure has on

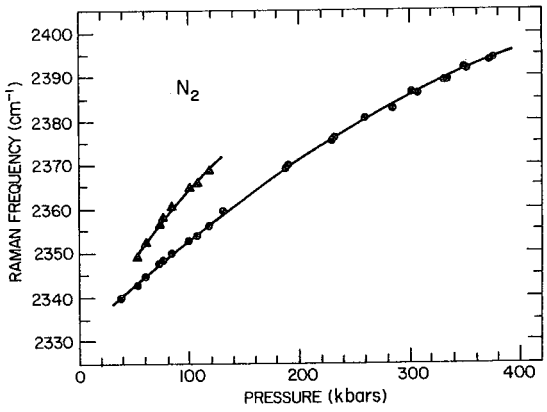

Fig. 8.36. The pressure dependence of internal-mode frequencies in crystalline N_2. After [8.117]

internal-mode frequencies. Over part of the pressure range, a Davydov doublet is observed whose separation (N_2-N_2 intermolecular interaction splitting) increases with pressure.

At this point, a few comments are in order about experimental techniques which have gone unmentioned thus far in our survey of results on molecular crystals. The spectroscopically-accurate but relatively low-pressure data of Figs. 8.32, 33, 35 were obtained with a Bridgman-type optical bomb in conjunction with a Daniels-type single-stage hydraulic press [8.29]. The data of Fig. 8.34 were obtained with a Drickamer-type optical cell [8.118]. The impressive measurements represented in Fig. 8.36 were made possible by recent advances in the use of the gasketed, ruby-calibrated, diamond-anvil cell (DAC) technique. The rest of the experimental results to be shown in subsequent figures have all been obtained by various versions of the DAC technique.

Thus far, we have given a sampling of some of the interesting recent results for this class of solid. In order to provide a degree of insight into how pressure acts upon the vibrational spectrum of a molecular solid and how this action differs significantly from that discussed earlier for covalent solids, it is necessary to pause in our survey and pick a specific material to discuss in some detail. A well-chosen concrete example allows us to display the salient points and also serves to lead into the physical model for these effects which is discussed in the following section.

The crystal chosen to serve this purpose is the molecular chalcogenide As_4S_4; its unit-cell structure is shown in Fig. 8.37. Over 30 phonon frequencies have been tracked under pressure for this inorganic molecular crystal, providing one of the most complete pictures thus far available for the effect of compression on the vibrational spectrum of *any* solid [8.108]. Within each As_4S_4 molecule, the bonding topology is readily understood and is concordant with the 8-*n* rule for covalent coordination. Each sulfur atom is bonded to two nearest-neighbor arsenics while each arsenic is bonded to three nearest neighbors, two of them sulfurs and the third an arsenic. The role of the As–As covalent bonds in the intramolecular structure is to cross-brace the As_4S_4 molecule to form a three-

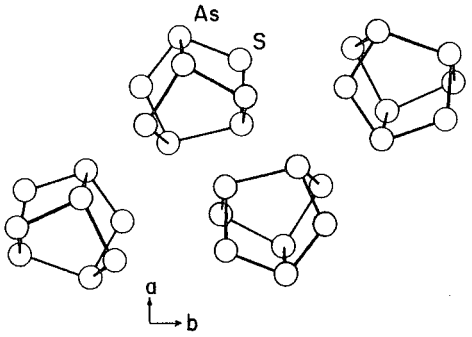

Fig. 8.37. Unit-cell structure of crystalline As_4S_4. Within each tightly-bound cage-like molecule, each As is covalently bonded to three neighbors and each S to two. When the atoms are fleshed out with their van der Waals radii, the As_4S_4 molecules appear nearly globular in shape

dimensional *cage-like* structure. This ensures a high degree of intramolecular rigidity; unlike sulfur with its open ring-like S_8 molecules, the rigid-molecule separation approximation is highly appropriate for crystalline As_4S_4.

As indicated in Fig. 8.37, there are four As_4S_4 molecules per unit cell. While this level of unit-cell complexity (32 atoms/cell) is not untypical for a molecular crystal, it is of course much more complex than the covalent semiconductors of Sect. 8.3. The following point must be strongly emphasized: *in contradiction to the conventional wisdom which holds that physicists must study simple systems to make progress, the unit-cell complexity of crystalline* As_4S_4 *is, in the present context, a blessing and not a curse.* The reason that this complexity is so welcome here is that, in combination with the low crystal symmetry ($P2_1/n$) and consequent generous selection rules for Raman activity, it allows us to monitor many modes in our pressure-Raman experiments. Direct optical access (via first-order Raman scattering) to numerous phonons of diverse frequencies distributed throughout the spectrum enables us to uncover global aspects of the response to pressure, as will be discussed in the following section.

The rich Raman spectrum of crystalline As_4S_4, at $P=0$ and at $P=39$ kbar, is shown in Fig. 8.38 [8.108]. These data, taken with the sample in a Bassett-type DAC [8.119] and using a near-infrared incident beam to which the crystal was transparent (the optical absorption edge of As_4S_4 is about 2.5 eV), show that quite clean spectra can be obtained with the anvil-cell technique even for low-frequency external-mode phonons. Unlike the spectra shown earlier, the spectra of Fig. 8.38 are complete in that they include both the external-mode and internal-mode regimes.

At $P=0$, the external modes in As_4S_4 fall at frequencies below 65 cm^{-1}. The internal modes fall into two clusters near 350 and 200 cm^{-1}, which may be roughly classified as intramolecular (covalent) bond-stretching and bond-bending modes, respectively. Some of the pressure-induced frequency shifts are indicated by horizontal arrows in Fig. 8.38, and the zero-pressure positions of the lines are given in parentheses above the frequency values observed at 39 kbar.

By far the most dramatic changes are those seen in the intermolecular regime. At 39 kbar, nearly all of the external modes have increased in frequency by about

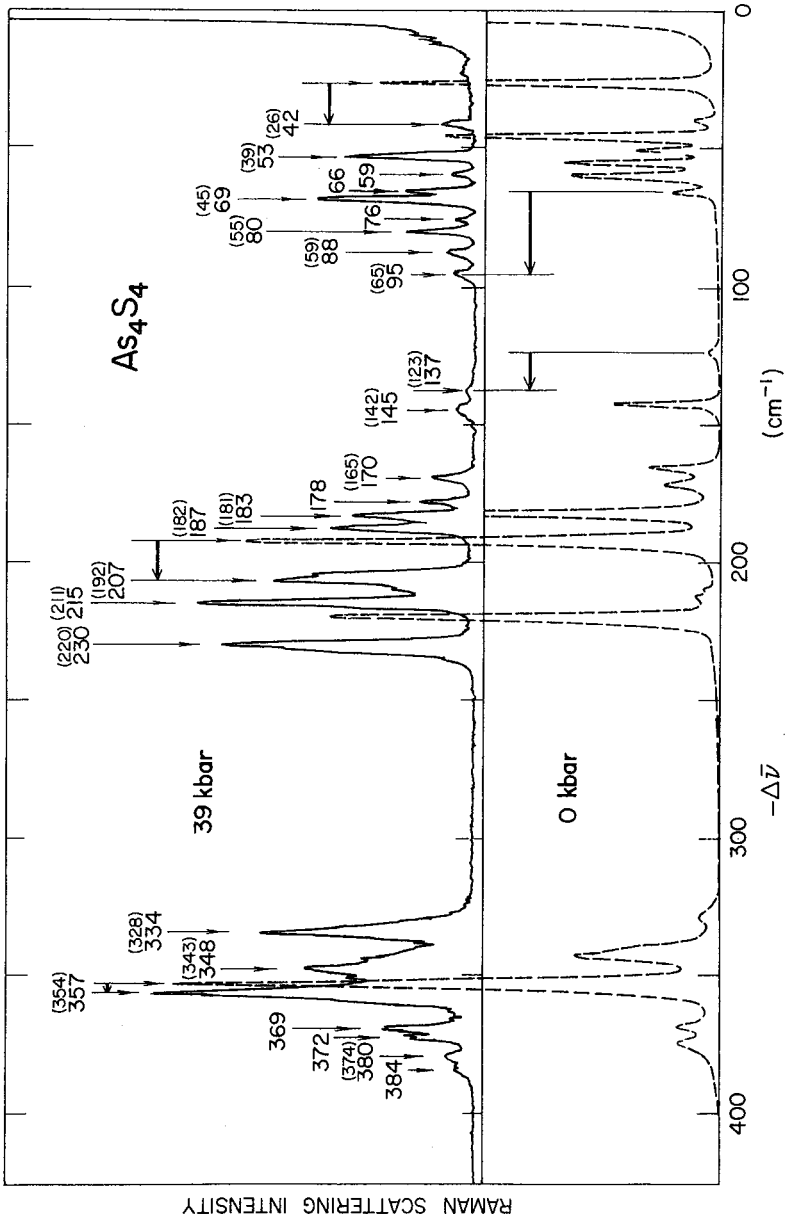

Fig. 8.38. The effect of pressure on the Raman spectrum of crystalline As_4S_4. For a few lines, the pressure-induced frequency shift is indicated by a heavy horizontal arrow. Line positions at 39 kbar are given in cm^{-1}, with the corresponding zero-pressure positions given in parentheses. After [8.108]

50 %. A by-now familiar consequence of this spectral expansion of the lattice-phonon regime is that new lines, hidden at $P=0$ by their proximity to stronger bands, are uncovered at high pressure. The response to pressure of the internal modes is markedly milder. The fractional increase for the bond-bending modes near 200 cm^{-1} is typically 5 %, and for the bond-stretching modes near 350 cm^{-1} the shift is a mere per cent or two.

These changes of frequency with pressure – very swift for the external-mode phonons, sluggish for the lower-frequency group of internal-mode phonons, and very sluggish for the upper group of internal-mode phonons – conspire to close the gaps in the spectrum. In particular, the important gap which separates the intermolecular from the intramolecular vibrations is strongly affected as the highest external mode rapidly gains on the lowest internal mode. As discussed in the following section which continues the analysis of these data, this gap closing under pressure is naturally interpreted in terms of the action of pressure in *selectively* stiffening (via bond shortening) the softest springs in the system. Pressure makes a molecular crystal *less molecular* in character by acting to diminish the intramolecular/intermolecular force-constant disparities.

8.7.3 Vibrational Scaling and the Systematics of the Response to Pressure

The pressure dependence of the phonon spectrum of As_4S_4, as exhibited in Fig. 8.38, is vastly different from the behaviour seen in network solids such as the covalent semiconductors. It is well to step back briefly and mention the usual expectation for the effect of pressure. First recall that, in the harmonic approximation, there is no effect whatsoever; ideal springs shorten, but do not stiffen, under compression. But because of the anharmonicity of the potential acting on atoms in real crystals, phonon frequencies do of course change with pressure. The simplest description for this is in terms of the Grüneisen approximation [8.19,20] and a simple sketch of this picture is shown in Fig. 8.39.

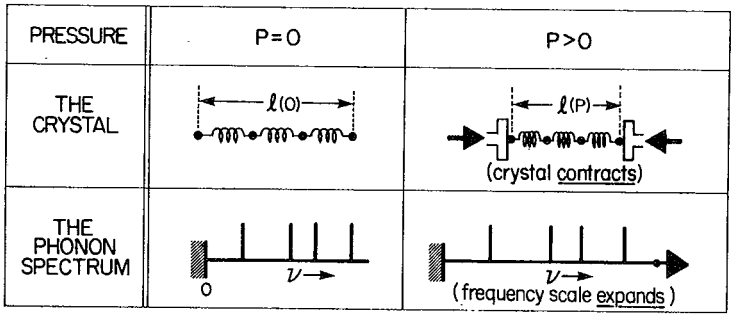

Fig. 8.39. Schematic representation of the scaling relation embodied by the Grüneisen approximation

For mode i in a crystal under compression, the mode-Grüneisen parameter γ_i is the dimensionless quantity connecting the volume dilatation $\Delta V/V$ with the consequent fractional change in phonon frequency, $\Delta\nu_i/\nu_i = \gamma_i(\Delta V/V) = \gamma_i \beta P$. In the Grüneisen approximation, all of the γ_i are assumed to be equal: $\gamma_i = \gamma$, independent of i. This is what is pictorially represented in Fig. 8.39. Pressure produces not only a contraction of the crystal in real space, but also a *uniform expansion of the spectrum in frequency space*. It is as if the spectrum were on a rubber band which experiences a tensile stress when the crystal is subjected to compressive stress. The Grüneisen picture amounts to a phenomenological scaling relationship between frequency and volume: $\nu \sim V^{-\gamma}$.

The Grüneisen model works fairly well as a zeroth-order view of the overall effect of pressure on vibrational frequencies in many materials, especially solids (such as the $3d$-network covalent semiconductors) in which a single type of bond controls the crystal dynamics. But we shall now show that it does *not* work for molecular solids, for which it fails in very striking fashion.

Figure 8.40 displays a compact representation of the pressure-Raman results of *Zallen* and *Slade* [8.108] on crystalline As_4S_4. *Each individual point* in this plot corresponds to a Raman-active zone-center phonon whose frequency has been followed as a function of pressure. The horizontal coordinate of the point is set by the zero-pressure frequency $\nu(P=0)$. The vertical coordinate is set by the initial $(P=0)$ logarithmic pressure derivative $(1/\nu)(d\nu/dP)$, with the value of $d\nu/dP$ at $P=0$ determined from $\nu(P)$ plots of the type shown in Figs. 8.32, 34. There are 31 points in Fig. 8.40, representing a wealth of information about the

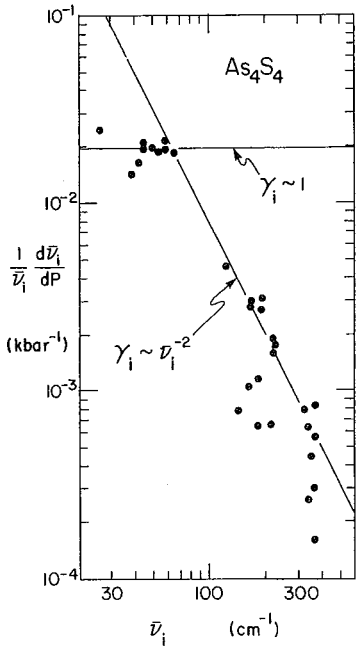

Fig. 8.40. Correlation between pressure sensitivity and phonon frequency for crystalline As_4S_4. Each point represents a phonon whose frequency has been tracked under pressure. After [8.108]

pressure dependence of the phonon spectrum. This wealth is based, as noted earlier, on the structural complexity of crystalline As_4S_4, which generously provides optical accessibility to many phonons. Since a search for systematic trends is the main object of Fig. 8.40, this *benefit derived from complexity* is of appreciable value here. (Contrast Fig. 8.40 with the corresponding plots for the first-order spectrum in diamond and NaCl. For diamond, the plot contains a single point, making it difficult to discern spectral trends. For NaCl, of course, the field is totally blank).

The Grüneisen approximation predicts, for Fig. 8.40, a set of points all lying on or near a horizontal line. Instead, we see that the mode-Grüneisen parameters span an extended range covering two orders of magnitude. Only within the confines of the external-mode manifold at low frequencies do the γ_i values cluster about the same level. As soon as the intramolecular regime is entered at higher frequency, the values observed for $(1/v)(dv/dP)$ rapidly plummet.

This drastic and systematic departure from Grüneisen scaling is a direct reflection of the *disparity of force constants which coexist in a molecular solid.* When pressure is applied to a solid in which very stiff springs and very soft springs coexist (schematically, as in Fig. 8.30), it is the soft springs which give. Most of the compression which occurs in a molecular solid is borne by the weak intermolecular bonds; the strong bonds within the molecule are relatively unaffected. Both types of bonds stiffen as they shorten (via their intrinsic anharmonicity), but since the strong bonds are shortened only slightly, their stiffening is also relatively slight.

A simple model for all of this, obtained with the aid of the elementary molecular-crystal model of Fig. 8.30, has been described earlier by one of the authors [8.106]. The basic assumption is that, although we must abandon $\nu_i \sim V^{-\gamma}$ (with γ independent of i) for molecular crystals, the idea of a basic vibrational scaling law can be salvaged in the form of the *bond-stiffness/bond-length* microscopic-scale statement $k \sim r^{-6\gamma}$. Here k is the force constant, r is the bond length and γ is a bond-scaling parameter of order unity which is presumed to apply to *both* intermolecular and intramolecular bonds. The last point treats the scaling exponent γ as a "universal" quantity, valid throughout the extended hierachy of bond strengths.

For the elementary model of Fig. 8.30c, $k \sim r^{-6\gamma}$ yields the following mode-Grüneisen parameters for the three zone-center phonons: for ω_1, $\gamma_i \approx 2\gamma$; for ω_0, $\gamma_i \approx (k_1/k_0)2\gamma$; for $\omega_0 + \Delta\omega$, $\gamma_i \approx (k_1/k_0)4\gamma$ [Ref. 8.106, Fig. 7]. The main point to observe is that for the internal modes, γ_i is reduced by a factor of order k_1/k_0 relative to γ_i of the external mode. A subsidiary point is that pressure increases the Davydov splitting of the internal-mode doublet, upshifting the higher line somewhat more than the lower one.

The generalization of the overall behavior displayed by the model is indicated by means of the two lines shown on Fig. 8.40 [8.108]. Within the low-frequency region populated by the external modes, Grüneisen scaling prevails (γ_i constant and of order unity) because the dynamics are dominated by a single bond type, namely, van der Waals. The flagrant fall-off which follows for the

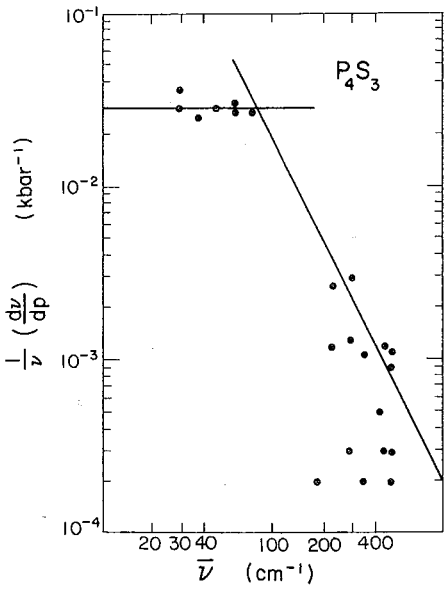

Fig. 8.41. Plot similar to that of Fig. 8.40, observed for crystalline P_4S_3. After [8.110]

internal modes is approximately bounded by an inverse-square correlation between pressure sensitivity and mode frequency: $\gamma_i \sim \nu_i^{-2}$. This follows from $\nu_i \sim k_i^{1/2}$ and $\gamma_i \sim k_i^{-1}$. It also follows that *the range of magnitudes spanned by the observed mode-Grüneisen parameters in a molecular crystal directly reflects the range of force constants which coexist in such a solid.* Thus, pressure-Raman experiments probe the hierarchy of bonding interactions which characterizes a molecular solid.

The broad features of the correlation between γ_i and ν_i, as described above and illustrated by As_4S_4 in Fig. 8.30, has now been seen in a variety of molecular crystals. Figure 8.41 shows recent results obtained by *Chattopadhyay* et al. [8.110] on crystalline P_4S_3. Other crystals for which this overall behavior has been confirmed include S_8 [8.106], S_4N_4 [8.108], $C_{10}F_8$ [8.109] and several organic compounds based on TCNQ [8.111].

8.7.4 The Connection Between the Effects of Pressure and Temperature

A valuable by-product of pressure-Raman experiments is the opportunity to separate the volume-driven ("implicit") and phonon-occupation driven ("explicit") components of the shifts in phonon frequencies which occur when *temperature* changes. Temperature is more subtle in its effect than pressure. A change in pressure alters the equilibrium interatomic spacings. A change in temperature, in addition to its effect on the vibrational excursions of the atoms about their equilibrium positions, *also* alters the interatomic spacings because of thermal expansion. The influence of temperature at constant pressure (normally

$P=0$) consists of two distinct contributions:

$$\left(\frac{\partial \nu}{\partial T}\right)_P = \left(\frac{\partial \nu}{\partial T}\right)_V - \left(\frac{\alpha}{\beta}\right)\left(\frac{\partial \nu}{\partial P}\right)_T \tag{8.19}$$

Here α and β are, respectively, the volume expansivity $(1/V)(\partial V/\partial T)_P$ and the compressibility $-(1/V)(\partial V/\partial P)_T$.

The left side of this equation is the total observed temperature coefficient, usually written simply $d\nu/dT$. The first term on the right is the "explicit" contribution at constant volume; it reflects the effect of the change in vibrational amplitudes, i.e., the phonon occupation numbers, at fixed equilibrium positions. The second term $-(\alpha/\beta)(d\nu/dP)$, known as the "implicit" contribution, reflects the effect of the change in equilibrium interatomic spacings which accompanies, via thermal expansion, a change in temperature. This equation has been discussed in some depth in [Ref. 8.108, Sect. VI.A]. One point worth emphasizing is that the equation evaporates in the absence of anharmonicity. For a perfectly harmonic solid (of which there are none), every quantity vanishes except for β.

The explicit/implicit mix in $d\nu/dT$ is a matter of intrinsic interest since it is needed for a proper interpretation of the observed influence of temperature on the phonon spectrum. For example, the limiting situation in which the implicit effect is totally dominant corresponds to the validity of the "quasi-harmonic approximation" [8.120] in which V is viewed as the single essential variable controlling ν. Exploiting recent pressure-Raman results, an analysis of the explicit/implicit dissection of temperature derivatives has been given by *Zallen* and *Conwell* [8.121]. Their compilation of experimental information on external modes in molecular crystals is presented in Figs. 8.42, 43.

Figures 8.42, 43 display the correlation between the temperature and pressure sensitivities of external-mode frequencies in three inorganic and three organic molecular crystals. Each point represents a Raman-active mode; it is positioned according to the pressure (x-axis) and temperature (y-axis) derivatives of the mode frequency near $P=0$ and $T=300$K. Experimental uncertainties are typically $\pm 10\%$ for $d\nu/dP$, $\pm 20\%$ for $d\nu/dT$. The reason that pressure derivatives are usually better determined than temperature derivatives lies in the greater scope available for pressure-induced shifts in ν, relative to temperature-induced shifts, making it easier to determine the slope of $\nu(P)$ than that of $\nu(T)$. To see this, note that it typically takes a temperature decrease of about 50K to produce the same upshift in frequency as that produced by a pressure increase of 1 kbar.

The straight lines passing through the origin in these figures are lines of constant explicit/implicit mix. Each of these "isomix" lines is labeled by the value of the dimensionless parameter η, the *implicit fraction* specifying the ratio of the volume-driven term $-(\alpha/\beta)(d\nu/dP)$ to the total temperature dependence $d\nu/dT$. Among the various possibilities for η, two cases are of special interest. Lines corresponding to the volume driven "purely-implicit" $\eta=1$ case have slopes equal to α/β in Figs. 8.42, 43, the expansivity/compressibility ratio for the crystal

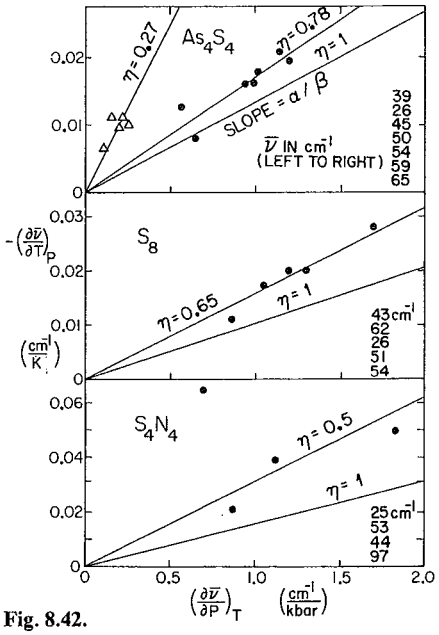

Fig. 8.42.

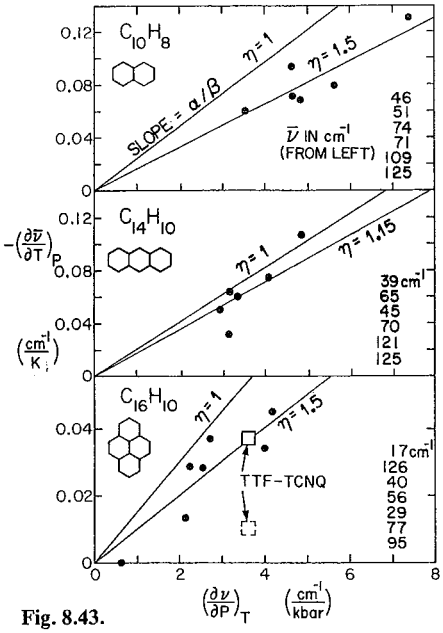

Fig. 8.43.

Fig. 8.42. The correlation between the temperature and pressure derivatives of phonon frequencies in three inorganic molecular crystals. Each point represents an external mode whose frequency has been followed as a function of temperature (at $P \approx 0$) and of pressure (at $T \approx 300$ K). The mode frequencies $\nu(P=0,\ T=300\,\text{K})$, corresponding to the points in sequence from left to right, are listed for each solid. Straight lines define loci of constant explicit/implicit mix in dv/dT, and are labeled by the implicit fraction η. For As_4S_4, the behavior of several bond-stretching internal modes (shown by the open triangles) is included for comparison. After [8.121]

Fig. 8.43. Temperature and pressure derivatives of intermolecular phonon frequencies in three organic crystals. Format is the same as in Fig. 8.42, but the scales are more extended because these modes are more sensitive to T and P. After [8.121]

in question. The opposite situation, in which the phonon-occupation-driven explicit effect dominates ($\eta = 0$), corresponds to the vertical axes. Other types of behavior, such as exact cancellation between effects of opposite sign ($\eta = \infty$), are indicated in Table 8.4 [8.121].

Figures 8.42, 43 indicate that, for external modes in molecular crystals, a definite correlation exists between the effects of temperature and pressure. The points scatter about lines with η values varying between 0.65 for sulfur to 1.5 for naphthalene and pyrene. The overall tendency certainly corresponds better to $\eta \approx 1$ than to either $\eta \approx 0$ or $\eta \approx \infty$. The data demonstrate that, to a reasonable approximation, *the volume-driven implicit effect dominates the temperature dependence of external-mode frequencies in molecular crystals.*

At the present time, it is not possible to compile a collection of results for internal modes as extensive as that presented for external modes in Figs. 8.42, 43.

Table 8.4. The physical composition of the temperature derivative of phonon frequency, and provisional conclusions for the connection with crystal bonding [8.121]

Physical situation	Composition of $-d\nu/dT$: Total = exp + imp	Implicit fraction η	Crystal-bonding class and mode type
(a) Phonon-occupation driven explicit effect dominates	1 = 1 + 0	0	Covalent crystals, internal modes in molecular crystals
(b) Comparable contributions of the same sign	1 = 0.5 + 0.5	0.5	
(c) Thermal-expansion-driven implicit effect dominates, validity of the quasiharmonic approx. ("volume is everything")	1 = 0 + 1	1	Ionic crystals, external modes in molecular crystals
(d) Implicit effect dominates, small explicit term of the opposite sign	1 = −0.5 + 1.5	1.5	
(e) Cancellation, no net effect of temperature	0 = −1 + 1	∞	

There is relatively little reliable information about the small temperature coefficients of the high-frequency phonons in molecular crystals. However, we may again make use of the comprehensive study [8.108] available for that paradigmatic molecular solid, crystalline As_4S_4. The relevant data are contained in the top panel of Fig. 8.42. In addition to the results on seven external modes (the solid dots, which lie quite close to the isomix line $\eta = 0.8$), results are also shown for five bond-stretching internal modes represented by the open triangles in this figure. These intramolecular modes reveal different behavior than the intermolecular ones; they are characterized by an implicit fraction of about $\eta = 0.3$. Another well-documented case is SnI_4 [8.122], which behaves similarly. Thus, unlike the situation for external modes, for internal modes the phonon-occupation driven explicit effect makes a significant contribution to the total temperature effect.

It is of significant interest to compare the conclusions arrived at here for molecular solids, for the explicit/implicit mix in $d\nu/dT$, with the temperature behavior of phonon frequencies in the two other major classes of insulating solids: ionic and covalent. This comparison, for the physical composition of the temperature derivative of phonon frequency, is summarized in Table 8.4 in somewhat oversimplified fashion.

For ionic solids, a substantial body of data [8.123] exists. It demonstrates that the thermal-expansion-dominated "volume-is-everything" limit gives an accurate description of $d\nu/dT$. This is the same conclusion as that reached here for intermolecular modes in molecular solids. There is a key physical similarity

between vibrations in ionic crystals and external-mode ($\approx$rigid-molecule) vibrations in molecular crystals; vibrations in both cases involve relative motions of electronically-nonoverlapping closed-shell entities.

Relatively few analyses of the makeup of dv/dT have been carried out for covalent semiconductors [8.124]. The sparse data suggest that the explicit and implicit effects are comparable in size, perhaps with a tendency for the explicit effect to be the larger one. The similarity here is evidently to the behavior of internal modes in molecular crystals, a similarity which seems natural enough because the intramolecular bonding is, after all, covalent. In both cases there is substantial charge overlap between the vibrating units.

8.7.5 Molecular-Nonmolecular Transitions at High Pressure

This chapter has been largely divided along class lines, with two distinct classes of solids (covalent and molecular) being separately treated and discussed. In a very real sense, this closing section bridges that division. Very high pressure severely blurs the distinction between covalent interactions and intermolecular ones, and this section addresses that phenomenon.

Eventually, all materials should go metallic at sufficiently high pressure. In the high density limit, electronic delocalization signals the triumph of kinetic energy over potential energy in a now-familiar story in condensed-matter physics (the Wigner lattice, the Mott transition, Anderson localization, etc.). One well-known scenario for this, although thus-far unrealized (at least on this planet), is the predicted appearance at very high pressure of a metallic solid based on monatomic hydrogen. Metallic hydrogen is the motivation of an active search in several high-pressure laboratories.

Figure 8.44 displays recent pressure-Raman results of *Sharma* et al. [8.28] on solid hydrogen up to 630 kbar. As in the case of the work on solid nitrogen discussed earlier, lattice modes could not be seen and the study focused on a covalent-bond-stretching internal mode. However, there is a remarkable difference between the behavior seen in Fig. 8.44 for solid H_2 and that shown earlier in Fig. 8.36 for solid N_2. The H–H intramolecular-stretch frequency turns over above 300 kbar and begins to *decrease*. This softening of the covalent bond within each H_2 molecule, as the molecules are forced to tightly pack together at high pressure, is suggestive of precursor behavior providing advance notice of the predicted transition to metallic hydrogen (which may take place in the 2–5 Mbar range [8.125]).

Molecular→nonmolecular transition phenomena under pressure are nicely seen in two types of molecular solids which have not yet been mentioned here. In all of the molecular crystals discussed thus far, the covalently-bonded unit (H_2, S_8, As_4S_4, etc.) is microscopic, i.e., finite on an atomic scale. There are many molecular crystals composed of macromolecules, covalently-bonded networks that are *macroscopically* extended in one dimension (*chain-structure* polymeric crystals such as polyethylene or trigonal Se) or in two dimensions (*layer-structure* crystals such as MoS_2 or GaSe). From the viewpoint of the macroscopic *network*

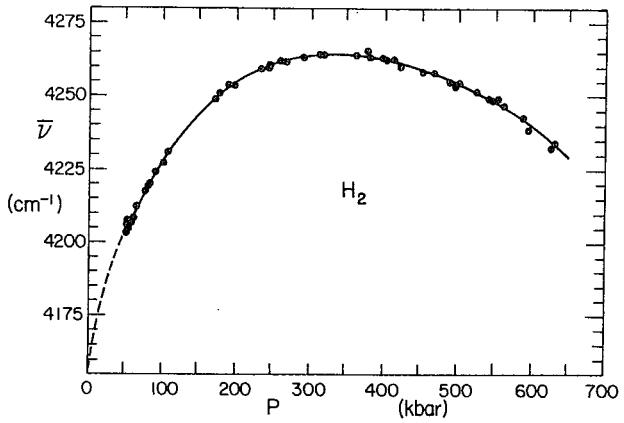

Fig. 8.44. The pressure dependence of an internal-mode frequency in crystalline H_2. Note the softening of the H – H intramolecular bond above 300 kbar. After [8.28]

dimensionality [8.126] of the covalently-bonded molecular unit, chain-structure Se is an example of a *1d network solid* and layer-structure MoS_2 is an example of a *2d network solid*. These two types of solids are *intermediate* in bonding topology between the two types of solids discussed earlier: *0d network* molecular solids (H_2, S_8) and *3d network* covalent solids (Si, Ge).

Trigonal selenium is an elemental polymer composed of helical chains (three atoms per turn, the simplest helix) packed in hexagonal array. Because of the extreme structural and chemical simplicity of this $1d$ network solid, its vibrational properties have been theoretically investigated in several studies, of which those most relevant to our discussion are the studies of *Martin* and co-workers [8.127]. Already at $P=0$, the separation approximation is invalid and the intermolecular (i.e., *interchain*) coupling contains some appreciable covalent-bonding character. Pressure increases the mixing between the intrachain and interchain bonding, with the result that the chain-chain bonds develop substantial covalent character and at the same time the primary (intrachain) bonding substantially *weakens*. Packing the chains more closely together causes a transfer of bonding charge from the intrachain to the interchain bonding [8.127, 128]. Thus pressure effects a molecular→nonmolecular crossover in this system.

Experimental support for the above picture is seen in the effect of pressure on the three Raman-active phonons in Se. Pressure-Raman experiments were first reported by *Richter* et al. [8.57], and then extended to 140 kbar (where Se undergoes a phase transition to a metallic form) by *Aoki* et al. [8.129] whose data are shown in Fig 8.45. The interesting feature is the pronounced *decrease* with pressure of the frequency of the A_1 internal mode, which is the symmetric-stretch "breathing" mode of the helical chain. The softening of this mode under pressure demonstrates the large pressure-induced decrease of the force constant associated with the intrachain covalent bond.

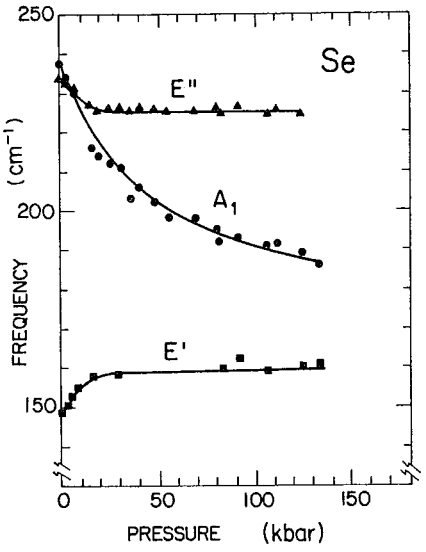

Fig. 8.45. The pressure dependence of the three Raman modes in trigonal Se. Note the pronounced drop in the frequency of the chain-breathing A_1 mode, which announces the pressure-induced weakening of the intrachain covalent bond. After [8.129]

Several two-dimensional network layer-structure crystals have been the subject of pressure-Raman investigations, including As_2S_3 [8.106, 130], GeS [8.131], GeSe [8.131], BN [8.132]. GaS [8.133] and GaSe [8.134]. In layer crystals, the vibrations corresponding to the external modes of ordinary (0*d* network) molecular solids are *rigid-layer* modes [8.135]. *Polian* et al. [8.133] have observed a rigid-layer mode in GaS from zero pressure up to 150 kbar. It experiences an enormous fractional change in frequency (from 23 to 76 cm^{-1}), corresponding to an order-of-magnitude enhancement of the interlayer interaction.

The pressure-induced molecular→nonmolecular crossover described above for chain-structure selenium amounts to a $1d \rightarrow 3d$ transition from the viewpoint of the covalent-bonding network dimensionality [8.126]. We close this chapter with a brief description of an analogous phenomenon in a layer-structure crystal, namely, $2d \rightarrow 3d$ dimensionality effects observed at high pressure by *Besson* et al. [8.130] for crystalline As_2S_3. This material, whose optical properties at zero pressure have been intensively investigated, is notable as the layer crystal for which the crucial role of the *diperiodic symmetry* (the proper factor-group symmetry of an individual $2d$ network macromolecule) was first appreciated and analyzed [8.136]. The dominance of the diperiodic symmetry at $P=0$ (and, conversely, the minor *subsidiary* role played by the conventional, triperiodic, crystal symmetry) is now well established for both the vibrational and electronic optical properties of this material. In brief, the observation of many degenerate or near-degenerate Raman-infrared line pairs, incomprehensible from the viewpoint of the crystal symmetry, is well explained on the basis of the diperiodic layer symmetry [8.136].

Besson et al. [8.130], in pressure-optical experiments on crystalline As_2S_3 to 100 kbar, have observed an intralayer Raman quadruplet which disperses

rapidly as the dominance of the diperiodic symmetry is broken at high pressure and the admixture repulsion of modes of like *crystal* symmetry forces them apart. They also saw a forbidden-crossover repulsion, enforced by crystal symmetry, of another pair of intralayer modes which were well separated in frequency at $P=0$ but attempted to cross at high pressure. These observations, along with the rapid rise in frequency of the rigid-layer modes (which become inextricably admixed with intralayer modes by 100 kbar), are clear evidence of $2d \rightarrow 3d$ molecular→nonmolecular pressure-induced effects.

Acknowledgements. The authors wish to take this opportunity to express their appreciation to Michael L. Slade for his essential contributions to much of the work reviewed here on molecular solids. In addition, we are greatly indebted to Cathyrn A. Horeth for her able and patient help in the preparation of this manuscript.

References

8.1 C.H.Whitfield, E.M.Brody, W.A.Bassett: Rev. Sci. Instrum. **47**, 942 (1976)
8.2a M.Cardona: Surf. Sci. **37**, 100 (1973)
M.Cardona: In *Atomic Structure and Properties of Solids*, ed. by E.Burstein (Academic Press, New York 1972) pp. 514–580
8.2b M.Cardona, G.Güntherodt (eds.): *Light Scattering in Solids II*, Topics Appl. Phys., Vol. 50 (Springer, Berlin, Heidelberg, New York 1982)
8.3 W.Hayes, R.Loudon: *Scattering of Light by Crystals* (Wiley, New York 1978) Chap. 1
8.4 B.A.Weinstein, M.Cardona: Phys. Rev. B7, 2545 (1973); Solid State Commun. **10**, 961 (1972)
8.5 P.A.Temple, C.E.Hathaway: Phys. Rev. B7, 3685 (1973)
8.6 L.N.Ovander: Opt. Spectrosc. **9**, 302 (1960)
8.7 R.Loudon: Advan. Phys. **13**, 423 (1964)
8.8 R.M.Martin, L.M.Falicov: In *Light Scattering in Solids I*, 2nd. ed., ed. by M.Cardona, Topics Appl. Phys., Vol. 8 (Springer, Berlin, Heidelberg, New York 1983) Chap. 3
8.9 H.Wendel: Solid State Commun. **31**, 423 (1979)
8.10 S.S.Mitra: In *Optical Properties of Solids*, ed. by S.Nudelman, S.S.Mitra (Plenum Press, New York 1969) pp. 378–451
8.11 M.Nicol, J.R.Kessler, Y.Ebisuzaki, W.D.Ellenson, M.Fong, C.S.Gratch: Dev. Appl. Spectrosc. **10**, 79 (1972)
8.12 P.S.Peercy: In *High-Pressure and Low-Temperature Physics*, ed. by C.W.Chu, J.A.Woollam (Plenum Press, New York 1977) p. 279
P.S.Peercy: In *Light Scattering in Solids*, ed. by M.Balkanski, R.C.C.Leite, S.P.S.Porto (Flammarion, Paris 1976) p. 782
8.13 J.R.Ferraro: Coordination Chem. Rev. **29**, 1 (1979)
8.14 W.F.Sherman, G.R.Wilkinson: In *Advances in Infrared and Raman Spectroscopy*, Vol. 6, ed. by R.J.H.Clark, R.E.Hester (Heyden, London 1980) Chap. 4
8.15 G.Martinez: In *Handbook on Semiconductors*, Vol. 2, ed. by T.S.Moss, M.Balkanski (North-Holland, Amsterdam 1980) Chap. 4c
8.16 M.Blackman: Proc. Phys. Soc. Lond. B**70**, 827 (1957)
8.17 W.B.Daniels: In *Lattice Dynamics*, ed. by R.F.Wallis (Pergamon Press, Oxford 1965) p. 273
8.18 P.Debye: Phys. Z. **14**, 259 (1913)
8.19 E.Grüneisen: In *Handbuch der Physik*, Vol. 10, ed. by Geiger and Scheels (Springer, Berlin 1926) Chap. 1
8.20 J.C.Slater: *Introduction to Chemical Physics*, (McGraw-Hill, New York 1939) pp. 217–240
8.21 J.S.Dugdale, D.K.Macdonald: Phys. Rev. **89**, 832 (1953)
8.22 T.Soma: Solid State Commun. **34**, 375 (1980); **34**, 927 (1980)

8.23 O.L.Anderson: Science **213**, 76 (1981)
8.24 G.J.Piermarini, S.Block: Rev. Sci. Instrum. **46**, 973 (1975)
J.D.Barnett, S.Block, G.J.Piermarini: Rev. Sci. Instrum. **44**, 1 (1973)
8.25 C.E.Weir, E.R.Lippincott, A. van Valkenburg, E.N.Bunting: J. Res. Natl. Bur. Stand. A**63**, 55 (1959)
8.26 R.A.Forman, G.J.Piermarini, J.D.Barnett, S.Block: Science **176**, 284 (1972)
8.27 B.A.Weinstein, G.J.Piermarini: Phys. Rev. B**12**, 1172 (1975)
8.28 S.K.Sharma, H.K.Mao, P.M.Bell: Phys. Rev. Lett. **44**, 886 (1980)
8.29 O.Brafman, S.S.Mitra, R.K.Crawford, W.B.Daniels, C.Postmus, J.R.Ferraro: Solid State Commun. **7**, 449 (1969)
8.30 J.M.Besson, J.P.Pinceaux: Rev. Sci. Instrum. **50**, 541 (1979)
8.31 D.M.Adams, S.J.Payne, K.Martin: Appl. Spectrosc. **27**, 377 (1973)
8.32 M.Nicol, Y.Ebisuzaki, W.D.Ellenson, A.Karim: Rev. Sci. Instrum. **43**, 1368 (1972)
8.33a H.K.Mao, P.M.Bell: Science **200**, 1145 (1978)
H.K.Mao, P.M.Bell, K.J.Dunn, R.M.Chrenko, R.C.Devries: Rev. Sci. Instrum. **50**, 1002 (1979)
8.33b A.Jayaraman: Rev. Mod. Phys. **55**, 65 (1983)
8.34 R.P.Lowndes: In *Proc. 4th Intern. Conf. on High Pressure*, Kyoto, 1974, ed. by J.Osugi (The Physico-Chemical Society of Japan, Kyoto 1975) p. 805
8.35 R.A.Noack, W.B.Holzapfel: In *High Pressure Science and Technology*, Vol. 1, ed. by K.D.Timmerhaus, M.S.Barber (Plenum Press, New York 1979) p. 748
8.36 M.Born, K.Huang: *Dynamical Theory of Crystal Lattices* (Oxford University Press, New York 1954) Chap. 2
8.37 C.J.Buchenauer, F.Cerdeira, M.Cardona: In *Light Scattering in Solids*, ed. by M.Balkanski (Flammarion, Paris 1971) p. 280
8.38 S.S.Mitra, O.Brafman, W.B.Daniels, R.K.Crawford: Phys. Rev. **186**, 942 (1969)
8.39 B.J.Parsons, C.D.Clark: In *Light Scattering in Solids*, ed. by M.Balkanski, R.C.C.Leite, S.P.S.Porto (Flammarion, Paris 1976) p. 414
8.40 K.Asaumi, S.Minomura: J. Phys. Soc. Japan-Lett. **45**, 1061 (1978)
8.41 B.A.Weinstein, G.J.Piermarini: Phys. Lett. **48**A, 14 (1974)
8.42a R.Trommer, H.Muller, M.Cardona, P.Vogl: Phys. Rev. B**21**, 4869 (1980)
8.42b D.Olego, M.Cardona, P.Vogl: Phys. Rev. B**25**, 3878 (1982);
J.A.Sanjurjo, E.Lopez-Cruz, P.Vogl, M.Cardona: (in press)
8.43a O.Brafman, S.S.Mitra: In *Light Scattering in Solids*, ed. by M.Balkanski (Flammarion, Paris 1971) p. 284
8.43b S.S.Mitra, K.V.Namjoshi: J.Chem. Phys. **55**, 1817 (1971)
8.44 R.Trommer, E.Anastassakis, M.Cardona: In *Light Scattering in Solids*, ed. by M.Balkanski, R.C.C.Leite, S.P.S.Porto (Flammarion, Paris 1976) p. 396
8.45 B.A.Weinstein, R.Zallen, M.L.Slade, A.deLozanne: Phys. Rev. B**24**, 4652 (1981)
8.46 W.A.Harrison, S.Ciraci: Phys. Rev. B**10**, 1516 (1974)
W.A.Harrison: Phys. Rev. B**8**, 4487 (1973); **14**, 702 (1976)
8.47 P.Vogl: J. Phys. C**11**, 251 (1978)
8.48 J.C.Phillips: Rev. Mod. Phys. **42**, 317 (1970)
J.A.VanVechten: Phys. Rev. **182**, 891 (1969)
8.49 V.Heine, R.O.Jones: J. Phys. C**2**, 719 (1969)
8.50 K.Kunc, R.M.Martin: Phys. Rev. B**24**, 2311 (1981); Phys. Rev. Lett. **48**, 406 (1982)
R.M.Martin, K.Kunc: Phys. Rev. B**24**, 2081 (1981)
8.51 H.Bilz, W.Kress: *Phonon Dispersion Relations in Insulators*, Springer Ser. Solid-State Sci., Vol. 10, (Springer, Berlin, Heidelberg, New York 1979) pp. 95–121
8.52 W.Richter, J.B.Renucci, M.Cardona: Solid State Commun. **16**, 131 (1975)
8.53 B.A.Weinstein, J.B.Renucci, M.Cardona: Solid State Commun. **12**, 473 (1973)
8.54 B.A.Weinstein: Solid State Commun. **24**, 595 (1977)
B.A.Weinstein: In *High Pressure Science and Technology*, Vol. 1, ed. by K.D.Timmerhaus, M.S.Barber (Plenum Press, New York 1979) p. 141
8.55 M.Zigone, R.Beserman, H.D.Fair,Jr.: In *Light Scattering in Solids*, ed. by M.Balkanski, R.C.C.Leite, S.P.S.Porto (Flammarion, Paris 1976) p. 597

8.56 D.N.Talwar, M.Vandevyver, K.Kunc, M.Zigone: Phys. Rev. B**24**, 741 (1981)
8.57 W.Richter, J.B.Renucci, M.Cardona: phys. stat. sol. (b) **56**, 223 (1973)
8.58 O.Brafman, M.Cardona, Z.Vardeny: Phys. Rev. B**15**, 1081 (1977)
8.59 Z.Vardeny, O.Brafman: Phys. Rev. B**19**, 3290 (1979)
8.60 D.S.Rimai, R.J.Sladek: Solid State Commun. **30**, 591 (1979)
8.61 B.A.Weinstein: In *Proc. 13th Intern. Conf. on the Physics of Semiconductors*, Rome, 1976, ed. by F.G.Fumi (North-Holland, Amsterdam 1976) p. 326
8.62 Y.S.Touloukian, R.K.Kirby, R.E.Taylor, T.Y.R.Lee: *Thermal Expansion*, Thermophysical Properties of Matter, Vol. 13, ed. by Y.S.Touloukian, C.Y.Ho (Plenum Press, New York 1977)
8.63 J.F.Vetelino, S.S.Mitra, K.V.Namjoshi: Phys. Rev. B**2**, 967 (1970)
8.64 G.Dolling, R.A.Cowley: Proc. Phys. Soc. Lond. **88**, 463 (1966)
8.65 R.M.Pick, M.H.Cohen, R.M.Martin: Phys. Rev. B**1**, 910 (1970)
R.M.Martin: Phys. Rev. **186**, 871 (1969)
8.66 R.D.Turner, J.C.Inkson: J. Phys. C**11**, 3961 (1978)
8.67 W.Porod, P.Vogl, G.Bauer: J. Phys. Soc. Japan (Suppl. A) **49**, 649 (1980)
8.68 M.T.Yin, M.L.Cohen: Phys. Rev. Lett. **45**, 1004 (1980); J. Phys. Soc. Japan (Suppl. A) **49**, 13 (1980); Solid State Commun. **38**, 625 (1981)
8.69 K.Maschke, W.Andreoni: J. Phys. Soc. Japan (Suppl. A) **49**, 745 (1980)
8.70 H.Jex: phys. stat. sol. (b) **45**, 343 (1971)
8.71 A.Bienenstock: Philos. Mag. **9**, 755 (1964)
8.72 J.C.Phillips: Phys. Rev. **166**, 832 (1968)
8.73 F.Herman: J. Phys. Chem. Sol. **8**, 405 (1959)
8.74 W.Weber: Phys. Rev. Lett. **33**, 371 (1974); Phys. Rev. B**15**, 4789 (1977)
8.75 J.Ihm, A.Zunger, M.L.Cohen: J. Phys. C**12**, 4409 (1979)
8.76 R.W.Shaw: Phys. Rev. **174**, 769 (1968)
8.77 H.Wendel, R.M.Martin: Phys. Rev. B**19**, 5251 (1979)
8.78 B.A.Weinstein: Solid State Commun. **20**, 999 (1976)
8.79 A.S.Barker,Jr.: Phys. Rev. **165**, 917 (1968)
8.80 W.Cochran, R.A.Cowley: In *Handbuch der Physik*, Vol. 25/2a, ed. by S.Flügge, L.Genzel (Springer, Berlin, Heidelberg, New York 1967) p. 118
8.81 J.Ruvalds, A.Zawadowski: Phys. Rev. B**2**, 1172 (1970)
8.82 J.L.Yarnell, J.L.Warren, R.G.Wenzel, P.J.Dean: In 4th *I.A.E.A. Symp. on Neutron Inelastic Scattering*, Vol. 1 (Intern. Atomic Energy Agency, Vienna 1968) p. 301
8.83 M.L.Shand, H.D.Hochheimer, M.Krauzman, J.E.Potts, R.C.Hanson, C.T.Walker: Phys. Rev. B**14**, 4637 (1976)
R.C.Hanson, M.L.Shand: In *High Pressure Science and Technology*, Vol. 1, ed. by K.D.Timmerhaus, M.S.Barber (Plenum Press, New York 1979) p. 453
8.84a Z.Vardeny, O.Brafman: Phys. Rev. B**19**, 3276 (1979)
8.84b D.Schmeltzer, R.Beserman: J. Phys. C**15**, 4173 (1982)
8.85 W.Klement, A.Jayaraman: In *Progress in Solid State Chemistry*, Vol. 3, ed. by H.Reiss (Pergamon Press, London 1966) p. 289
8.86 S.C.Yu, I.L.Spain, E.F.Skelton: Solid State Commun. **25**, 49 (1978)
M.A.Baublitz, Jr., A.L.Ruoff: J. Appl. Phys. **53**, 6179 (1982)
8.87 B.Henion, F.Moussa, B.Prevot, C.Carabatos, C.Schwab: Phys. Rev. Lett. **28**, 964 (1972)
8.88 Y.Ebisuzaki, M.Nicol: J. Phys. Chem. Sol. **33**, 763 (1971)
8.89 R.C.Hanson, T.A.Fjeldly, H.D.Hochheimer: Phys. Stat. Sol. (b) **70**, 567 (1975)
8.90 C.Carlone, D.Olego, A.Jayaraman, M.Cardona: Phys. Rev. B**22**, 3877 (1980)
8.91 H.G.Drickamer: In *Solid State Physics*, **17**, 1 (Academic Press, New York 1965) and references therein
S.Minomura, G.A.Samara, H.G.Drickamer: J. Appl. Phys. **33**, 3196 (1962)
8.92 J.C.Jamieson: Science **139**, 762 (1963); **139**, 845 (1963)
8.93 J.S.Kasper, S.M.Richards: Acta Crystallogr. **17**, 752 (1964)
R.H.Wentorf, Jr., J.S.Kasper: Science **139**, 338 (1963)
8.94a M.T.Yin, M.L.Cohen: Phys. Rev. B**26**, 5668 (1982); Phys. Rev. Lett. **50**, 1172 (1983); J.Ihm, M.L.Cohen: Phys. Rev. B**23**, 1576 (1981)

8.94b S.Froyen, M.L.Cohen: Phys. Rev. B**28**, 3258 (1983); Solid State Commun. **43**, 447 (1982)
8.94c E.J.Mele, J.D.Joannopoulos: Phys. Rev. B**24**, 3145 (1981)
8.95 J.C.Phillips: Phys. Rev. Lett. **27**, 1197 (1971); Phys. Rev. B**25**, 2310 (1982)
8.96 D.Olego, M.Cardona: Phys. Rev. B**25**, 1151 (1982)
8.97 P.Y.Yu, B.Welber: Solid State Commun. **25**, 209 (1978)
8.98 R.E.Hanneman, M.D.Banus, H.C.Gatos: J. Phys. Chem. Sol. **25**, 293 (1964)
8.99 M.J.P.Musgrave: Proc. R. Soc. A**272**, 503 (1963)
8.100 H.H.Demarest,Jr., R.Ota, O.L.Anderson: In *High-Pressure Research*, ed. by M.H.Manghnani, S.Akimoto (Academic Press, New York 1977) p. 281
8.101 J.C.Phillips: *Bonds and Bands in Semiconductors* (Academic Press, New York 1973) p. 93
8.102 W.Richter, R.Zeyher, M.Cardona: Phys. Rev. B**18**, 4312 (1978)
8.103 E.Anastassakis, F.H.Pollak, G.W.Rubloff: Phys. Rev. B**9**, 551 (1974)
8.104 E.M.Anastassakis: In *Dynamical Properties of Solids*, Vol. 4, ed. by G.K.Horton, A.A.Maradudin (North-Holland, New York 1980) pp. 221–227
8.105 B.Welber, M.Cardona, C.K.Kim, S.Rodriguez: Phys. Rev. B**12**, 5729 (1975)
8.106 R.Zallen: Phys. Rev. B**9**, 4485 (1974)
8.107 G.S.Pawley, S.J.Cyvin: J. Chem. Phys. **52**, 4073 (1970)
8.108 R.Zallen, M.L.Slade: Phys. Rev. B**18**, 5775 (1978)
8.109 D.M.Adams, A.C.Shaw, G.A.Mackenzie, G.S.Pawley: J. Phys. Chem. Sol. **41**, 149 (1980)
8.110 T.Chattopadhyay, C.Carlone, A.Jayaraman, H.G. von Schnering: Phys. Rev. B**23**, 2471 (1981)
8.111 C.Carlone, N.K.Hota, H.J.Stolz, M.Elbert, H.D.Hochheimer: J. Chem. Phys. **75**, 3220 (1981)
8.112 P.W.Bridgman: Proc. Am. Acad. Arts Sci. **72**, 227 (1938)
8.113 R.Zallen, C.H.Griffiths, M.L.Slade, M.Hayek, O.Brafman: Chem. Phys. Lett **39**, 85 (1976)
8.114 W.D.Ellenson, M. Nicol: J. Chem. Phys. **61**, 1380 (1974)
8.115 E.Whalley, A.Lavergne, P.T.T.Wong: Rev. Sci. Instrum. **47**, 845 (1976)
8.116 J.V.E.Kurittu: Physica Scripta **21**, 194 (1980); **21**, 200 (1980)
8.117 R.LeSar, S.A.Ekberg, L.H.Jones, R.L.Mills, L.A.Schwalbe, D.H.Schiferl: Solid State Commun. **32**, 131 (1979)
8.118 An excellent review of the various pressure-Raman techniques has been given in [8.14]
8.119 W.A.Bassett, T.Takahashi, P.W.Stook: Rev. Sci. Instrum. **38**, 37 (1967)
8.120 G.Liebfried, W.Ludwig: Solid State Phys. **12**, 275 (1961)
8.121 R.Zallen, E.M.Conwell: Solid State Commun. **31**, 557 (1979)
8.122 P.S.Peercy, G.A.Samara, B.Morosin: J. Phys. Chem. Sol. **36**, 1123 (1975)
8.123 S.S.Mitra, C.Postmus, J.R.Ferraro: Phys. Rev. Lett. **18**, 455 (1967)
C.Postmus, J.R.Ferraro, S.S.Mitra: Phys. Rev. **174**, 983 (1968)
J.F.Asell, M.Nicol: J. Chem. Phys. **49**, 5395 (1968)
R.P.Lowndes: J. Phys. C**4**, 3083 (1971)
P.S.Peercy, B.Morosin: Phys. Rev. B**7**, 2779 (1972)
J.A.Taylor, M.S.Haque, J.B.Page,Jr., C.T.Walker: Phys. Rev. B**12**, 5969 (1975)
8.124 H.D.Hochheimer, M.L.Shand, J.E.Potts, R.C.Hanson, C.T.Walker: Phys. Rev. B**14**, 4630 (1976)
D.G.Mead, G.R.Wilkinson: J. Raman Spectrosc. **6**, 123 (1977)
8.125 J. van Straaten, R.J.Wijngaarden, I.F.Silvera: Phys. Rev. Lett. **48**, 97 (1982)
8.126 R.Zallen: In *Proc. Enrico Fermi Summer School on Lattice Dynamics and Intermolecular Forces*, Varenna, 1972 (Academic Press, New York 1975) p. 159; and in *Proc. 12th Intern. Conf. Physics of Semiconductors*, Stuttgart (Teubner, Stuttgart 1974) p. 621
8.127 R.M.Martin, G.Lucovsky, K.Helliwell: Phys. Rev. B**13**, 1383 (1976)
R.M.Martin, T.A.Fjeldly, W.Richter: Solid State Commun. **18**, 865 (1976)
R.M.Martin, G.Lucovsky: In *Proc. 12th Intern. Conf. Physics of Semiconductors*, Stuttgart (Teubner, Stuttgart 1974) p. 184
8.128 J.D.Joannopoulos, M.Schluter, M.L.Cohen: Phys. Rev. B**11**, 2186 (1975)
8.129 K.Aoki, O.Shimomura, S.Minomura, N.Koshizuka, T.Tsushima: J. Phys. Soc. Japan **48**, 906 (1980)
8.130 J.M.Besson, J.Cernogora, R.Zallen: Phys. Rev. B**22**, 3866 (1980)
8.131 H.R.Chandrasekhar, R.G.Humphreys, M.Cardona: Phys. Rev. B**16**, 2981 (1977)

8.132 T.Kuzuba, Y.Sato, S.Yamaoka, K.Era: Phys. Rev. **B18**, 4440 (1978)
8.133 A.Polian, J.C.Chervin, J.M.Besson: Phys. Rev. **B22**, 3049 (1980)
8.134 E.A.Vinogradov, G.N.Zhizhin, N.N.Melnik, S.I.Subbotin, V.V.Panfilov, K.R.Allakhverdiev, S.S.Babaev, V.F.Zhitar: Phys. Stat. Sol. (b) **99**, 215 (1980)
8.135 R.Zallen, M.L.Slade: Phys. Rev. **B9**, 1627 (1974)
8.136 R.Zallen, M.L.Slade, A.T.Ward: Phys. Rev. **B3**, 4257 (1971)

Bibliography of References Concerning Raman Scattering by Phonons Under Uniaxial Stress

Stress-induced shifts of first-order Raman frequencies of diamond- and zinc-blende-type semiconductors:
F.Cerdeira, C. J.Buchenauer, F. H.Pollak: Phys. Rev. **B5**, 580 (1972)

Piezospectroscopic study of the Raman spectrum of α-quartz:
V. J.Tekippe, A.K.Ramdas, S.Rodriguez: Phys. Rev. **B8**, 706 (1973)

Effect of uniaxial stress on the Raman spectra of cubic Crystals: CaF_2, BaF_2, and $Bi_{12}GeO_{20}$:
S.Venugopalan, A.K.Ramdas: Phys. Rev. **B8**, 717 (1973)

Effects of uniaxial stress on resonance Raman scattering near the E_1-gaps in InSb and InAs:
E.Anastassakis: 11th Intern. Conf. on Physics of Semiconductors (PAN, Warsaw 1972) p. 227

Elastic constants and Raman frequencies of heavily-doped Si under uniaxial stress:
T.A.Fjeldly, F.Cerdeira, M.Cardona: Solid State Commun. **12**, 553 (1973)

Effect of uniaxial stress and doping on the one-phonon Raman spectrum of GaP:
I.Balslev: Phys. Stat. Sol. (b) **61**, 207 (1974)

Effect of free carriers on zone-center vibrational modes in heavily doped p-type Si. II. Optical modes:
F.Cerdeira, T.A.Fjeldly, M.Cardona: Phys. Rev. **B8**, 4734 (1973)

Uniaxial stress dependence of the Raman-active phonons in TiO_2:
P.S.Peercy: Phys. Rev. **B8**, 6018 (1973)

Effects of uniaxial stress on the Raman frequencies of Ti_2O_3 and Al_2O_3:
S.H.Shin, F.Pollak, P.M.Raccah: J. Solid State Chem. **12**, 294 (1975)

Temperature and pressure dependences of the properties and phase transition in paratellurite: ultrasonic, dielectric, and Raman and Brillouin scattering results:
P.S.Peercy, I.J.Fritz, G.A.Samara: J. Phys. Chem. Solids **36**, 1105 (1975)

Effect of uniaxial stress on the unstable phonon in ferroelectric gadolinium molybdate:
B.N.Ganguly, F.G.Ullman, R.D.Kirby, J.R.Hardy: Phys. Rev. **B12**, 3783 (1975)

Stress-induced ferroelectricity and soft phonon modes in $SrTiO_3$:
H. Uwe, T. Sakudo: Phys. Rev. B**13**, 271 (1976)

Resonant Raman scattering under uniaxial stress: $E_1 - E_1 + \Delta_1$ gaps:
W. Richter, R. Zeyher, M. Cardona: In *Light Scattering in Solids*, ed. by M. Balkanski, R.C.C. Leite, S.P.S. Porto (Flammarion, Paris 1976) p. 63

Effects of uniaxial stress on the Raman frequencies of Ti_2O_3 and Al_2O_3:
S.H. Shin, F.H. Pollak, P.M. Raccah: In *Light Scattering in Solids*, ed. by M. Balkanski, R.C.C. Leite, S.P.S. Porto (Flammarion, Paris 1976) p. 401

Piezospectroscopic study of the Raman spectrum of cadmium sulfide:
R.J. Briggs, A.K. Ramdas: Phys. Rev. B**13**, 5518 (1976)

Effects of stress on the Raman spectra of Mg_2Si and Mg_2Sn:
S. Onari, M. Cardona, E. Schönherr, W. Stetter: Phys. Stat. Sol. (b) **79**, 269 (1977)

Raman-scattering study of stress-induced ferroelectricity in $KTaO_3$:
H. Uwe, T. Sakudo: Phys. Rev. B**15**, 337 (1977)

Piezospectroscopy of Raman lines exhibiting linear wave-vector dependence. Quartz:
M.H. Grimsditch, A.K. Ramdas, S. Rodriguez, V.J. Tekippe: Phys. Rev. B**15**, 5869 (1977)

Piezospectroscopy of the Raman spectrum of α-quartz:
R.J. Briggs, A.K. Ramdas: Phys. Rev. B**16**, 3815 (1977)

Effects off interband excitations on Raman phonons in heavily-doped n-Si:
M. Chandrasekhar, J.B. Renucci, M. Cardona: Phys. Rev. B**17**, 1623 (1978)

Self-energy of phonons interacting with free electrons in silicon:
M. Chandrasekhar, M. Cardona: In *Lattice Dynamics*, ed. by M. Balkanski (Flammarion, Paris 1978) p. 186

Lattice dynamics of paratellurite under uniaxial stress:
M.A.F. Scarparo, V. Lemos, R.S. Katiyar, F. Cerdeira: In *Lattice Dynamics*, ed. by M. Balkanski (Flammarion, Paris 1978) p. 707

Raman-scattering measurements and the effect of uniaxial stress on the ferroelectric transition in $Gd_2(MoO_4)_3$:
Q. Kim, F.G. Ullman, R.D. Kirby, and J.R. Hardy: In *Lattice Dynamics*, ed. by M. Balkanski (Flammarion, Paris 1978) p. 664

Linear wave-vector dependence of an optical phonon frequency in $Bi_{12}GeO_{20}$ in the vicinity of the Brillouin zone center:
W. Imaino, A.K. Ramdas, S. Rodriguez: Solid State Commun. **28**, 211 (1978)

Anomalous damping of phonons in ferroelectric $Gd_2(MoO_4)_3$:
Q. Kim, and F.G. Ullman: Phys. Rev. B**18**, 3579 (1978)

Resonance Raman scattering in semiconductors under uniaxial stress. E_1 ($E_1 + \Delta_1$) Gaps:
W. Richter, R. Zeyher, M. Cardona: Phys. Rev. B**18**, 4312 (1978)

Stress dependence of the zone-center optical phonons of LaF_3:
F. Cerdeira, V. Lemos, R.S. Katiyar: Phys. Rev. B**19**, 5413 (1979)

Intra- and interband Raman scattering in heavily-doped p-Si:
M. Chandrasekhar, U. Rössler, M. Cardona: In *The Physics of Semiconductors*, ed. by B.L.H. Wilson (Institute of Physics, London 1979) p. 961

Uniaxial-stress dependence of the first-order Raman spectrum of rutile. I. Experiments:
P. Merle, J. Pascual, J. Camassel, H. Mathieu: Phys. Rev. B**21**, 1617 (1980)

Uniaxial-stress dependence of the first-order Raman spectrum of rutile. II. Model calculation:
J. Pascual, J. Camassel, P. Merle, H. Mathieu: Phys. Rev. B**21**, 2439 (1980)

Raman scattering under uniaxial and hydrostatic stresses in $Ba_2NaNb_5O_{15}$ crystals:
J. Sapriel, A. Boudou, G. Martinez: Ferroelectrics **29**, 15 (1980)

Study of the localized vibrations of boron in heavily-doped Si:
M. Chandrasekhar, H.R. Chandrasekhar, H. Grimsditch, M. Cardona: Phys. Rev. B**22**, 4825 (1980)

Linear wave-vector dependence of optical phonon frequencies in bismuth germanium oxide in the vicinity of the Brillouin zone center:
W. Imaino, A.K. Ramdas, S. Rodriguez: Phys. Rev. B**22**, 5679 (1980)

Inelastic light scattering in the presence of uniaxial stresses:
E. Anastassakis: J. Raman Spectroscopy **10**, 64 (1981)

Uniaxial-stress dependence of the first-order Raman spectrum of rutile-type crystals. III. MgF_2:
J. Pascual, J. Camassel, P. Merle, B. Gil, H. Mathieu: Phys. Rev. B**24**, 2101 (1981)

Uniaxial stress dependence of the amplitude mode of K_2SeO_4 at 82K:
N.E. Massa, F.G. Ullman, J.R. Hardy: In *Proc. 7th Intern. Conf. on Raman Spectroscopy* (North-Holland, Amsterdam 1980) p. 64

Effect of uniaxial stress on the zone-center phonons of diamond:
M.H. Grimsditch, E. Anastassakis, M. Cardona: Phys. Rev. B**18**, 901 (1978)